

# Non-Reciprocal Interactions Reshape Topological Defect Annihilation

Ylann Rouzairé,<sup>1,2,\*</sup> Daniel J.G. Pearce,<sup>3</sup> Ignacio Pagonabarraga,<sup>1,2</sup> and Demian Levis<sup>1,2</sup>

<sup>1</sup>Departament de Física de la Materia Condensada,

Universitat de Barcelona, Martí i Franquès 1, E08028 Barcelona, Spain

<sup>2</sup>UBICS University of Barcelona Institute of Complex Systems, Martí i Franquès 1, E08028 Barcelona, Spain

<sup>3</sup>Université de Genève Département de physique théorique,

24 quai Ernest-Ansermet, 1211 Genève, Switzerland

(Dated: June 14, 2024)

We show how non-reciprocal ferromagnetic interactions between neighbouring planar spins in two dimensions, affect the behaviour of topological defects. Non-reciprocity is introduced by weighting the coupling strength of the two-dimensional XY model by an anisotropic kernel. As a consequence, in addition to the topological charge  $q$ , the actual shape of the defects becomes crucial to faithfully describe their dynamics. Non-reciprocal coupling twists the spin field, selecting specific defect shapes, dramatically altering the pair annihilation process. Defect annihilation can either be enhanced or hindered, depending on the shape of the defects concerned and the degree of non-reciprocity in the system. We introduce a continuous description – for which the phenomenological coefficients can be explicitly written in terms of the microscopic ones – that captures the behaviour of the lattice model.

Collective excitations in the form of topological defects are known to control the large-scale behaviour of a broad class of equilibrium systems, and to be eventually responsible for a Kosterlitz-Thouless (KT) phase transition, as exhibited by the two-dimensional (2d) XY model [1–3]. Being local singularities of the relevant order parameter field, topological defects can be considered as quasi-particles (characterised by their charge  $q$ ), robust against perturbations [4–6], and the study of their dynamics provides insights into the ordering mechanisms at play [7–11]. Out-of-equilibrium, topological defects exhibit distinctive dynamical features, such as self-propulsion or super-diffusion, often breaking the symmetry between oppositely charged defects [12–20]. In active systems, for which their elementary constituents can self-generate stresses, the dynamics of defects has been recently identified with a growing number of biological processes [21–24]. Although the impact of defects on the critical properties of active matter is still to be settled [25–28], understanding their dynamics can clarify self-organisation mechanisms in living systems and eventually inspire the design of novel materials.

Non-reciprocal (NR) interactions provide an alternative route to conceive systems locally driven out-of-equilibrium. Indeed, the effective interactions between non-equilibrium agents generically violates the *actio-reactio* principle. Examples include microorganisms [29], social agents [30–34], catalytic colloids [35] or specifically tailored robot swarms [36–38]. The analysis of both particle and spin models, together with continuum theories, have recently shown that non-reciprocity leads to distinct emergent phenomena [20, 37, 39–51]. In particular, continuous theories of constant-density flocks *à la* Toner-Tu, should capture the large scale behaviour of non-reciprocal continuous spins [40, 51, 52].

In this manuscript we uncover the effect of NR interac-

tions on topological defects. We start from an extension of the 2dXY model where a given spin interacts with its neighbourhood in a way that depends on the state of the spin itself: interactions are stronger along the spins' heading direction. We show that NR interactions affect the shape of +1 isolated defects, which in turn impacts their annihilation kinetics and coarsening dynamics. We also introduce a continuum description which reproduces these results and gives a microscopic origin to the phenomenological coefficients in the Toner-Tu equation.

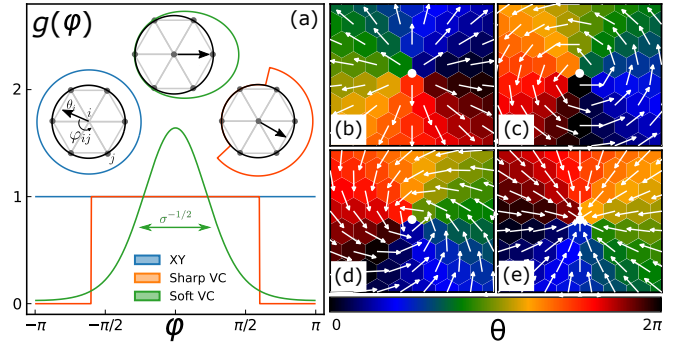


FIG. 1. (a) Sketch of the nearest neighbours coupling: the isotropic reciprocal case, in blue, the sharp vision cone, in orange, and our smooth version, in green (using  $\sigma = 5$ ). (b–e) Four +1 defects with  $\mu_+ =$  (b) 0, (c)  $\pi/2$ , (d)  $3\pi/4$ , (e)  $\pi$ . White dots show the defect core, on the dual (hexagonal) lattice. The colour code displays the phase  $\theta$  of each spin.

The NR 2dXY model is composed of spins  $\mathbf{S}_i = (\cos \theta_i, \sin \theta_i)$  sitting on the nodes of a triangular lattice of linear size  $L$ , and evolving accordingly to

$$\gamma \dot{\theta}_i = J \sum_{j \in \text{nn}_i} g_\sigma(\varphi_{ij}) \sin(\theta_j - \theta_i) + \sqrt{2\gamma T} \eta_i(t) \quad (1)$$

where  $\gamma$  is the damping coefficient,  $J$  the coupling,  $\eta$  a Gaussian white noise with zero mean and unit vari-

ance and  $T$  the temperature of the bath to which the system is coupled (fixing  $k_B = 1$ ). NR interactions are introduced by weighting the coupling between two neighbouring spins, say  $i$  and  $j$ , according to the orientation of spin  $i$  with respect to the direction of the bond connecting the two, denoted  $\varphi_{ij}$  (see sketch Fig.1(a)). This is encoded in the kernel  $g_\sigma$ : the reciprocal  $2dXY$  model with overdamped (non-conserved) dynamics [9] is recovered for constant  $g_\sigma$ , while “vision cone” interactions would correspond to a step function kernel [31, 48, 53]. We consider instead a “smooth vision cone”, based on the Von Mises distribution:  $g_\sigma(\varphi) = \exp(\sigma \cos \varphi)$  [54] to avoid several discretisation effects (discussed in the SM [55]) and allows considering other ways of breaking the action-reaction principle. As in the small  $\varphi$  regime  $g_\sigma(\varphi) \sim e^{-\varphi^2/2\sigma^{-1}}$ ,  $\sigma$  plays the role of the inverse variance (higher  $\sigma$  values shrink the vision cone).

The model is thus fully controlled by two non-dimensional parameters: the *reduced temperature*  $T \equiv T/J$ , and the *non-reciprocal parameter*  $\sigma \geq 0$ . Time is expressed in units of  $\gamma/J$ . Importantly, as  $g_\sigma(\varphi_{ij})$  depends on  $\theta_i$  but not  $\theta_j$ , Eq.(1) cannot be thought of as an equilibrium dynamics driven by a Hamiltonian-like function  $\mathcal{H} = -J \sum g_\sigma(\varphi_{ij}) \mathbf{S}_i \cdot \mathbf{S}_j$ . Indeed, in the presence of NR interactions the energy of a bond is ambiguous, as  $g_\sigma(\varphi_{ij}) \neq g_\sigma(\varphi_{ji})$ . Generally speaking, the defining feature of a NR system is its dynamics, that here we chose to be Langevin-like [15, 37] (contrary to Glauber type as in [48]). Thus,  $\sigma$  breaks *parity*,  $O(2)$  *rotational* and *time-reversal* symmetry [56, 57] (see SM[55]).

The  $2dXY$  model features point-like topological defects with integer charge,  $q$ , given by the winding number [4]. The local field around a defect located at the origin is given by  $\theta(x, y) = q \text{atan}(y/x) + \mu$ , where the integration constant  $\mu$  physically represents its *shape* (see Fig.1(b-e)). Building on this reference form, we define, in our NR model, the (scalar) shape of a defect as  $\mu = \text{Arg}(\sum_{j=1}^3 e^{i[\theta_j - q \text{atan}(y_j/x_j)]})$ , where the sum runs over the sites defining the plaquette in which the defect lies. For  $q = -1$  defects,  $\mu_-$  corresponds to a global rotation of the defect by  $\mu_-/2$ . However, for  $q = +1$  defects  $\mu_+$  changes the shape of the defect, giving *sources* ( $\mu_+ = 0$ ), *sinks* ( $\mu_+ = \pm\pi$ ) and *vortices* ( $\mu_+ = \pm\pi/2$ ).

To understand the effect of NR interactions on  $\mu_+$  we analyse an isolated  $q = +1$  defect. We observe that at zero temperature, the source and sink are stationary states. All intermediate defect shapes decay to a sink, shown for  $\mu_+ = \pi/6$  in Fig. 2(a-c). By approximating the dynamics of  $\theta$  close to a defect, we show that  $\mu_+ = 0$  is an unstable fixed point and  $\mu_+ = \pi$  is stable, see SM [55]. To highlight the mechanism behind this effect, consider a  $q = +1$  vortex defect ( $\mu_+ = \pi/2$ ). The arrows in front of a given spin point slightly towards the defect core, and the arrows behind slightly away. In a reciprocal system, these influences balance and the defect shape is stable. NR interactions cause an imbalance between these two

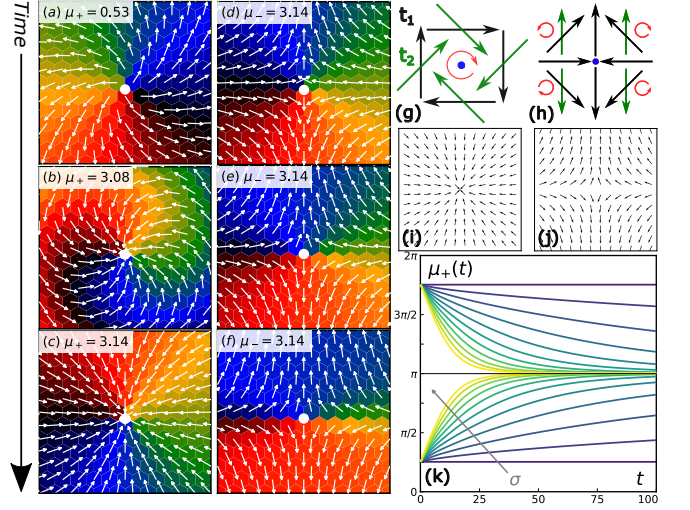


FIG. 2. (a,b,c) Twist of a positive defect towards the sink state ( $\mu_+ = \pi$ ). Same color code as in Fig.1. (d,e,f) Polarisation of a negative defect. (g,h) Reshaping mechanism for  $+1$  (g) and  $-1$  (h) defects, at time  $t_1$  (black) and  $t_2 > t_1$  (green). (i,j) Analytical final states computed in SM [55], for  $+1$  (i) and  $-1$  (j) defects. (k) Time evolution a  $q = +1$  defect's shape for different  $\sigma$  from 0 (dark blue) to 0.5 (yellow) by increments of 0.05, for two initial configurations ( $\mu_0 = \pi/4, 7\pi/4$ ).

influences leading to a torque on the spins, reshaping the defect as sketched in Fig.2(g).

To quantify such reshaping, we follow  $\mu_+(t)$  in time at  $T = 0$ . As expected, for  $\sigma = 0$ , the shape of the defect remains unchanged, see Fig.2(k). For  $\sigma > 0$ ,  $\mu_+$  spontaneously decays to  $\pi$  (sink), from any initial value  $\mu_0$ . While  $\sigma$  appears to control the decay rate, it does not define a characteristic timescale that can be used to collapse the curves. To gain some insight, we derive (cf. SM [55]) the following continuous approximation of Eq.(1) in a square lattice, at  $T = 0$ , for small  $\sigma$  and small spatial gradients:

$$\dot{\theta} = \Delta\theta + 2\sigma (\nabla \times \mathbf{S})_z \equiv f_{\text{EL}} + \sigma f_{\text{NR}} \quad (2)$$

where  $\Delta$  is the Laplacian operator and  $\mathbf{S}$  the spin vector field. From this expression, it is clear that  $\sigma$  cannot be absorbed in the time unit and that the dynamics are  $\mu_+$ -invariant around a  $q = 1$  defect if and only if  $\sigma = 0$ .

The reciprocal part of the kernel is responsible for the elastic force  $f_{\text{EL}}$  (the  $2dXY$  model in the spin wave approximation [5]) while the NR part, by explicitly introducing an asymmetry (here front/back), allows spins to be sensitive to the vorticity of the surrounding spin field. The resulting twisting torque  $f_{\text{NR}}$  powers the twist from the inside of the defect's core, where the amplitude of the rotational is greater. The elastic term distributes the stress isotropically, explaining why the twist radially propagates outwards, see Fig.2(b). Sinks are attractors of the dynamics, while sources are only unstable fixed

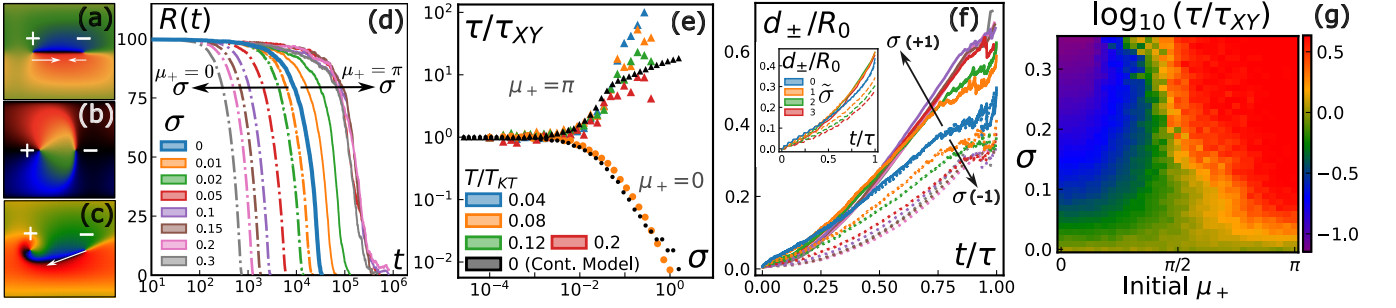


FIG. 3. (a,b,c) Configurations of two defects of opposite charge at  $T = 0, \sigma = 0.35$  with  $\mu_+ = 0, \pi, \pi/2$ , respectively. Arrows indicate their velocity. (d) Inter-defect distance  $R(t)$  between a  $\mu_+ = 0$  and a  $\mu_- = \pi$  (dashed lines) and a  $\mu_+ = \pi$  and a  $\mu_- = 0$  (solid lines) pair. In both cases,  $T = 0.08 T_{KT}, L = 2R_0 = 200$ . Sources enhance annihilation, sinks hinder it. (e) Annihilation time  $\tau$  rescaled by the one in the  $2dXY$  case, for  $\mu_+ = 0, \pi$  and different temperatures ( $L = 2R_0 = 100$ ). For the continuous model ( $L = 256$ ), we plot the data against  $2\tilde{\sigma}/L$  to compare to  $\sigma$  (cf. SM [55]). For  $\mu_+ = 0$ , we only display the case  $T = 0.08 T_{KT}$  as curves for different temperatures superimpose for all  $\sigma$ . (f) Distance travelled  $d_{\pm}/R_0$  by  $+1$  (solid lines) and  $-1$  (dotted lines) defects in the configuration shown in panel (a) ( $\mu_+ = 0, \mu_- = \pi$ ) for several values of  $\sigma$ , increasing in the direction of the arrows. Inset: same quantity for the continuous model, for  $\tilde{\sigma} = 0, 1, 2, 3$ . (g) Colour map of the annihilation time in log-scale as a function of initial shape  $0 \leq \mu_+ \leq \pi$  and non-reciprocity  $\sigma$  (using  $L = 64, R_0 = 30$  and  $T = 0.08 T_{KT}$ ).

points at  $T = 0$ ; thermal noise induces fluctuations in the field, generating a non-vanishing  $f_{NR}$ . Such twisting is also found in continuum theories of constant-density flocks [50].

We now turn our attention on  $q = -1$  defects. Figure 2(d) shows a stable  $q = -1$  defect in the absence of NR interactions. Here it is clear to see that the curl of the spin vector field has a quadrupole like symmetry, which will be reflected in  $f_{NR}$  (see SM [55]) and is highlighted in Fig.2(h). This results in a stable defect shape with a symmetry axis from which the spin vector points predominantly outwards (see Fig.2(f) for a numerical configuration and Fig.2(j) for the final stable shape obtained analytically). The existence and relevance at large scales of such structures has been studied by means of continuum models of constant-density flocks in [51]. Importantly, the polarised field around a  $q = -1$  defect provides a preferred path for defect motion. The location of the defect core can slide along the symmetry axis with a small, continuous variation of the spin vector field. On the contrary, it is very unfavourable for the defect to move perpendicular to the axis as it would require a large number ( $\sim L$ ) of spin flips.

As NR interactions reshape defects, they strongly impact their annihilation dynamics. In the reciprocal  $2dXY$  model, defects of opposite charge  $\pm q$  at a distance  $R$  attract each other with a Coulomb force  $F \sim q^2/R$  that drives their annihilation at low  $T < T_{KT} = 1.42$  [5, 9, 15, 16, 55]. The model is symmetric under parity and thus  $\pm q$  defects are equivalent. NR interactions break such symmetry, therefore can *enhance* or *hinder* the annihilation process and induce effective *transverse forces*, depending on the specific shape of the defects involved.

To explore the annihilation process, we study a pair

of defects of charge  $q = \pm 1$  and initial shapes  $\mu_{\pm}$  at a distance  $R_0$ , imposing periodic boundary conditions. To obtain a non-twisted initial configuration, we impose the *least distortion condition*  $\mu_- - \mu_+ = \pi$  (derived in the SM [55]). We then let the system evolve at  $T = 0.08 T_{KT}$  and track defects over time to obtain their displacement  $d_{\pm}(t)$  and their mutual distance  $R(t)$ . We focus first on two limit situations, involving sources and sinks, that will provide our reference scenarios, to then move to the description of more general annihilation process, as illustrated in Fig.3(a-c).

A source,  $\mu_+ = 0$ , can only be initially paired with a  $\mu_- = \pi$  defect that creates a symmetry axis along the core-to-core direction, see Fig.3(a). Such symmetry provides a preferential annihilation pathway. As shown in Fig.3(d),  $R(t)$  decays faster for larger values of  $\sigma$ , which translates into a reduced annihilation time  $\tau$  (that appears to be independent of  $T$ , see Fig.3(e)). Moreover,  $q = \pm 1$  defects are no longer equivalent:  $+1$  defects move faster than  $-1$  defects in the enhanced annihilation process (Fig.3(f)). This is in contrast with the equilibrium XY model, for which the invariance under the transformation  $\theta \rightarrow -\theta$  prevents any differentiation, and with the continuum theory studied by Vafa [50], where the defect interactions appear to be symmetric.

For a sink,  $\mu_+ = \pi$  ( $\mu_- = 0$ ), the symmetry axis of the  $-1$  defect grows perpendicular to the core-to-core direction, as illustrated in Fig.3(b). Such structure hinders the motion along the core-to-core direction, thus hindering annihilation. Since the formation rate of the symmetry axis increases linearly with  $\sigma$  (see [55]),  $R(t)$  exhibits a slower decay (solid lines in Fig.3(d)) and the annihilation is dramatically slowed down, up to a factor  $10^2$  with respect to the  $2dXY$  case, see Fig.3(e).

For any other initial pair, the  $+1$  defect experiences a



twist due to a non-vanishing  $f_{\text{NR}}$ , while the  $-1$  defect grows an oblique symmetry axis, that eventually curls to meet the  $+1$  defect core, see Fig. 3(c). Once the preferential path between the two defects has been created, the  $-1$  moves along it until either the defects are close enough to annihilate or the polarisation axis becomes perpendicular to the  $+1/-1$  direction.

The annihilation time (normalised by  $\tau_{XY}$ , the corresponding time in the  $2dXY$  model) for a pair of defects as a function of  $\mu_+$  and  $\sigma$  is shown in Fig. 3(g). As  $\sigma$  is increased, annihilation times are either increased for  $\mu_+ \approx \pi$  (red region) or decreased for  $\mu_+$  and large  $\sigma$  (blue region in Fig. 3(g)) with a smooth transition between the two extremes. Sharp vision cones give qualitatively similar results, confirming the robustness of our findings. By imposing the same head-tail asymmetry to both sharp and soft kernels, we obtain an equivalence relation between  $\sigma$  and the sharp vision cone aperture  $\Theta$  that gives a good quantitative agreement between both models [55]. At the coarsegrained level, our model can be described by

$$\dot{\mathbf{S}} = \Delta \mathbf{S} + \tilde{\sigma} (\nabla \times \mathbf{S}) \times \mathbf{S} + \alpha (1 - \mathbf{S}^2) \mathbf{S} \quad (3)$$

The first two terms directly derive from Eq. (2) (cf. SM [55]). Relaxing the spherical constraint  $|\mathbf{S}| = 1$ , the last Landau-like term enforces it with a Lagrange multiplier  $\alpha$ . Since  $(\nabla \times \mathbf{S}) \times \mathbf{S} = (\mathbf{S} \cdot \nabla) \mathbf{S} - \frac{1}{2} \nabla |\mathbf{S}|^2$ , the rotational term binds together the  $\propto (\mathbf{S} \cdot \nabla) \mathbf{S}$  self-advecting term and  $\propto \nabla |\mathbf{S}|^2$  term of the constant density Toner-Tu equation [58, 59]. Thus, our agent-based model provides a natural microscopic origin to the phenomenological coefficients in such field theories of flocking. In [50], the same twisting of isolated positive defects was found by just considering the self-advection term in the  $O(2)$  model, showing the robustness of this phenomenon. By setting  $\tilde{\sigma} = 2a\sigma$  ( $a$  is the lattice spacing), the numerical integration of Eq. (3) provides the same annihilation times as the lattice model once rescaled by the  $2dXY$  value. The continuum description also faithfully reproduces the asymmetry between the  $\pm 1$  defects' kinetics during annihilation (inset of Fig. 3(f)).

As NR interactions impact significantly the defect annihilation, it is worth exploring its consequences in the coarsening process. We thus analyse the relaxation following a quench from a disordered state, with a large number of defects, to very low temperatures, where only a few bonded defects might persist [10, 16, 60]. We show in Fig. 4(a) a snapshot of the system during its relaxation at  $T = 0$  and in Fig. 4(b) the time evolution of the defect density for different values of  $\sigma$  at  $T = 0.08 T_{KT}$ . Occasionally, defect pairs spontaneously generate to temporarily release local excessive forces, but the newly created defects rapidly annihilate (cf. [55] Movie 6b). As such, the steady state is typically defectless at such low temperatures, in agreement with the long-ranged ordered phase reported in a similar lattice model [48]. We did not find evidence for the metastability of the ordered state

reported in [51], that might be due to either differences between those two approaches or finite-size effects. Nevertheless, the coarsening of our system gets significantly slower for larger values of  $\sigma$ :  $+1$  defects quickly decay to sinks, giving rise to long lived *chains of sinks* (circles in Fig. 4(a)) separated by  $-1$  defects with symmetry axes that hinder annihilation with the nearest  $+1$  defects. In the  $2dXY$  model, those structures are highly unstable and thus never observed. Non-reciprocity stabilises those large-scale structures (cf. Supplementary Movies [55]), providing an explanation of the slowing down of the decay of the defect density.

To conclude, we have shown how NR interactions reshape topological defects in a paradigmatic continuous spin system. In short, non-reciprocity twists the phase field, breaking the parity and rotational symmetry of the  $2dXY$  model. In the regime of small deviations from homogeneity, non-reciprocity translates into a novel term in the continuum dynamical equation of the spin field, proportional to its vorticity. The impact of this new term is to segregate defects according to their specific shape (on top of their charge), leading to a rich phenomenology for pair annihilation. The latter can dramatically speed up or slow down, depending on the specific phase field between defects, resulting from the combination of the non-reciprocal twist and the generalised elasticity of the system. Such intricate scenario goes well beyond the isotropic annihilation of defects in the  $2dXY$  model, driven by an effective Coulomb interaction. While we cannot definitively rule out the possibility of describing these intricate dynamics more concisely and uniformly through an effective, anisotropic interaction between defects, in the spirit of Kosterlitz and Thouless theory, the scenario we have outlined appears to be more complex than what would result from simple pairwise forces. The present study of non-reciprocal defects opens new venues for the dynamical control of topological charges in non-equilibrium systems.

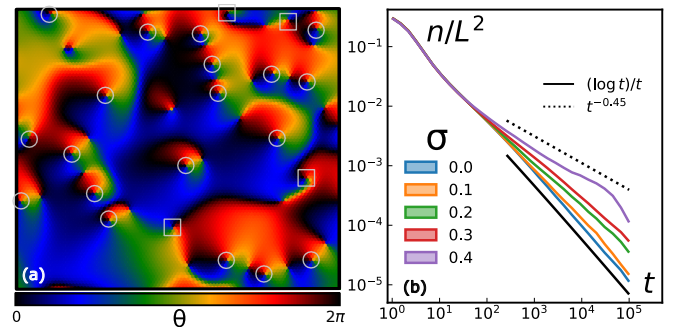


FIG. 4. (a) Snapshot of a  $L = 100$  system at  $t = 200, T = 0, \sigma = 0.3$ . Sink defects ( $q = +1, \mu_+ = \pi$ ) are circled. The other  $q = +1$  defects are squared (negative defects are not highlighted). (b) Time evolution of the defect density  $n/L^2$  for  $L = 200, T = 0.08 T_{KT}$  and different  $\sigma$ .

*Acknowledgements* D.L. and I.P. acknowledge DURSI for financial support under Project No. 2021SGR-673. I.P. and Y.R. acknowledge support from Ministerio de Ciencia, Innovación y Universidades MCIU/AEI/FEDER for financial support under grant agreement PID2021-126570NB-100 AEI/FEDER-EU. D.L. acknowledges MCIU/AEI for financial support under grant agreement PID2022-140407NB-C22. I.P. acknowledges Generalitat de Catalunya for financial support under Program Icrea Acadèmia. D.J.G.P. acknowledges Swiss National Science Foundation for financial support under SNSF Starting Grant TMSGI2-211367. Y.R. thanks Elisabeth Agoritsas, Boris Bergsma and Filippo de Luca for fruitful discussions. Y.R., D.L. and I.P. thank Hugues Chaté and Alexandre Solon for pointing out relevant references and triggering fruitful discussions.

---

\* rouzaire.ylann@gmail.com

- [1] V. L. Berezinskii, Sov. Phys. JETP **32**, 493 (1971).
- [2] J. M. Kosterlitz and D. J. Thouless, J. Phys. C **6**, 1181 (1973).
- [3] J. M. Kosterlitz, J. Phys. C **7**, 1046 (1974).
- [4] N. D. Mermin, Rev. Mod. Phys. **51**, 591 (1979).
- [5] P. M. Chaikin, T. C. Lubensky, and T. A. Witten, Vol. 10 (Cambridge University Press, 1995).
- [6] D. R. Nelson, (Cambridge University Press, 2002).
- [7] T. W. Kibble, J. Phys. A: Math. Gen. **9**, 1387 (1976).
- [8] W. H. Zurek, Nature **317**, 505 (1985).
- [9] B. Yurke, A. Pargellis, T. Kovacs, and D. Huse, Phys. Rev. E **47**, 1525 (1993).
- [10] A. Jelic and L. Cugliandolo, J. Stat. Mech. Theory Exp. **2011** (2011).
- [11] D. J. G. Pearce and K. Kruse, Soft Matter **17**, 7408 (2021).
- [12] L. Giomi, M. J. Bowick, P. Mishra, R. Sknepnek, and M. C. Marchetti, Philos. Trans. Royal Soc. A **372**, 20130365 (2014).
- [13] D. Pearce, S. Gat, G. Livne, A. Bernheim-Groswasser, and K. Kruse, arXiv preprint arXiv:2010.13141 (2020).
- [14] L. Braverman, C. Scheibner, B. VanSaders, and V. Vitelli, Phys. Rev. Lett. **127**, 268001 (2021).
- [15] Y. Rouzaire and D. Levis, Phys. Rev. Lett. **127** (2021).
- [16] Y. Rouzaire and D. Levis, Front. Phys. **10**, 785 (2022).
- [17] S. Shankar, A. Souslov, M. J. Bowick, M. C. Marchetti, and V. Vitelli, Nat. Rev. Phys. **4**, 380 (2022).
- [18] E. S. Bililign, F. Balboa Usabiaga, Y. A. Ganan, A. Poncet, V. Soni, S. Magkiriadou, M. J. Shelley, D. Bartolo, and W. T. Irvine, Nat. Phys. **18**, 212 (2022).
- [19] A. Chardac, L. A. Hoffmann, Y. Poupard, L. Giomi, and D. Bartolo, Phys. Rev. X **11**, 031069 (2021).
- [20] A. Poncet and D. Bartolo, Phys. Rev. Lett. **128**, 048002 (2022).
- [21] T. B. Saw, A. Doostmohammadi, V. Nier, L. Kocgozlu, S. Thampi, Y. Toyama, P. Marcq, C. T. Lim, J. M. Yeomans, and B. Ladoux, Nature **544**, 212 (2017).
- [22] K. Kawaguchi, R. Kageyama, and M. Sano, Nature **545**, 327 (2017).
- [23] K. Copenhagen, R. Alert, N. S. Wingreen, and J. W. Shaevitz, Nat. Phys. **17**, 211 (2021).
- [24] Y. Maroudas-Sacks, L. Garion, L. Shani-Zerbib, A. Livshits, E. Braun, and K. Keren, Nat. Phys. **17**, 251 (2021).
- [25] P. Digregorio, D. Levis, L. F. Cugliandolo, G. Gonnella, and I. Pagonabarraga, Soft Matter **18**, 566 (2022).
- [26] S. Shankar, S. Ramaswamy, M. C. Marchetti, and M. J. Bowick, Phys. Rev. Lett. **121**, 108002 (2018).
- [27] D. Pearce, J. Nambisan, P. Ellis, A. Fernandez-Nieves, and L. Giomi, Phys. Rev. Lett. **127**, 197801 (2021).
- [28] X.-Q. Shi, F. Cheng, and H. Chaté, Phys. Rev. Lett. **131**, 108301 (2023).
- [29] J. Agudo-Canalejo and R. Golestanian, Phys. Rev. Lett. **123**, 018101 (2019).
- [30] P. A. Abrams, Annu. Rev. Ecol. Evol. Syst. **31**, 79 (2000).
- [31] I. D. Couzin, J. Krause, N. R. Franks, and S. A. Levin, Nature **433**, 513 (2005).
- [32] C. Castellano, S. Fortunato, and V. Loreto, Rev. Mod. Phys. **81**, 591 (2009).
- [33] R. Pastor-Satorras, C. Castellano, P. Van Mieghem, and A. Vespignani, Rev. Mod. Phys. **87**, 925 (2015).
- [34] V. Ros, F. Roy, G. Biroli, G. Bunin, and A. M. Turner, Phys. Rev. Lett. **130**, 257401 (2023).
- [35] J. Grauer, F. Schmidt, J. Pineda, B. Midtvedt, H. Löwen, G. Volpe, and B. Liebchen, Nat. Comm. **12**, 6005 (2021).
- [36] M. Rubenstein, A. Cornejo, and R. Nagpal, Science **345**, 795 (2014).
- [37] M. Fruchart, R. Hanai, P. B. Littlewood, and V. Vitelli, Nature **592**, 363 (2021).
- [38] D. March, J. Múgica, E. E. Ferrero, and M. C. Miguel, arXiv preprint arXiv:2310.15592 (2023).
- [39] A. Ivlev, J. Bartnick, M. Heinen, C.-R. Du, V. Nosenko, and H. Löwen, Phys. Rev. X **5**, 011035 (2015).
- [40] L. P. Dadhichi, J. Kethapelli, R. Chajwa, S. Ramaswamy, and A. Maitra, Phys. Rev. E **101**, 052601 (2020).
- [41] Z. You, A. Baskaran, and M. C. Marchetti, Proc. Natl. Acad. Sci. **117**, 19767 (2020).
- [42] S. Saha, J. Agudo-Canalejo, and R. Golestanian, Phys. Rev. X **10**, 041009 (2020).
- [43] M. Han, M. Fruchart, C. Scheibner, S. Vaikuntanathan, J. J. De Pablo, and V. Vitelli, Nat. Phys. **17**, 1260 (2021).
- [44] Y. Avni, M. Fruchart, D. Martin, D. Seara, and V. Vitelli, arXiv preprint arXiv:2311.05471 (2023).
- [45] A. Benois, M. Jardat, V. Dahirel, V. Démery, J. Agudo-Canalejo, R. Golestanian, and P. Illien, Phys. Rev. E **108**, 054606 (2023).
- [46] N. Rana and R. Golestanian, arXiv preprint arXiv:2306.03513 (2023).
- [47] D. J. Hickey, R. Golestanian, and A. Vilfan, Proc. Natl. Acad. Sci. **120** (2023).
- [48] S. A. Loos, S. H. Klapp, and T. Martynek, Phys. Rev. Lett. **130**, 198301 (2023).
- [49] D. S. Seara, A. Piya, and A. P. Tabatabai, J. Stat. Mech. Theory Exp. **2023**, 043209 (2023).
- [50] F. Vafa, Soft Matter **18**, 8087 (2022).
- [51] M. Besse, H. Chaté, and A. Solon, Phys. Rev. Lett. **129**, 268003 (2022).
- [52] A. Solon, Journal Club for Condensed Matter Physics , DOI:10.36471/JCCM December 2022 01 (2022).
- [53] Q. S. Chen, A. Patelli, H. Chaté, Y. Q. Ma, and X. Q. Shi, Phys. Rev. E **96**, 020601 (2017).
- [54] K. V. Mardia, P. E. Jupp, and K. Mardia, Vol. 2 (Wiley Online Library, 2000).

- [55] See Supplemental Material at doi:....  
 [56] S. A. M. Loos and S. H. L. Klapp, New J. Phys. **22**, 123051 (2020).  
 [57] T. Suchanek, K. Kroy, and S. A. Loos, arXiv preprint arXiv:2305.05633 (2023).  
 [58] J. Toner and Y. Tu, Phys. Rev. Lett. **75**, 4326 (1995).  
 [59] J. Toner, Y. Tu, and S. Ramaswamy, Ann. Phys. **318**, 170 (2005).  
 [60] F. Rojas and A. Rutenberg, Phys. Rev. E **60**, 212 (1999).  
 [61] M. Hasenbusch, J. Phys. A **38**, 5869 (2005).  
 [62] H. Weber and P. Minnhagen, Phys. Rev. B **37** (1988).  
 [63] P. Butera and M. Comi, Phys. Rev. B **50**, 3052 (1994).  
 [64] O. Chepizhko, D. Saintillan, and F. Peruani, Soft Matter **17**, 3113 (2021).

## CONTENTS

References	5
Supplementary Movies	6
Implementation details	8
Equation of motion : adimensionalisation procedure	8
Numerical Implementation of the Square and Triangular Lattices	9
Computation of the spatial correlation function	10
Constructing a pair of defects with controlled shapes	10
The defects' shape : definition, comments and analytic calculations	11
Stability of a +1 defect	13
Shape of a -1 defect	14
Numerical results	14
Symmetries of the system	14
Kosterlitz-Thouless Critical Temperature	15
Growth of the polarisation axis with $\sigma$	16
Derivation of Eq. (2) and Eq. (3)	16
Rewriting the model of Ref. [50] in terms of vector calculus operators	20
Supplementary discussion on the work of Loos, Klapp and Martynek (Phys. Rev. Lett. , 2023)	21
Discretisation issues	21
Small vision cones and percolation threshold	23
Comparison between sharp and soft vision cones	23
Soft vision cones	24
Sharp vision cones	24
Equation of motion stemming from the XY energy modulated by the kernel	24

## Supplementary Movies

We provide short movies to visualize the dynamics at play at the single defect level, at the pair level and finally at the system's level (unidirectional gradient propagation as reported in [48] and coarsening dynamics). All videos can be found on this Youtube channel.

It helps sketching the configuration to understand which spins are mainly influenced by which spins. Here is a correspondence that might help :

Black :  $\theta = 0$  ( $\rightarrow$ )

Blue :  $\theta = \pi/2$  ( $\uparrow$ )

Green/yellow :  $\theta = \pi$  ( $\leftarrow$ )

Red/orange :  $\theta = 3\pi/2 = -\pi/2$  ( $\downarrow$ )

### Single defects

Both movies are at  $T = 0, \sigma = 0.3$ .

- “1- Twist” :  
movie of the twist of a positive defect with an initial shape  $\mu_+(t = 0) = 1$ . The final state is a sink, easily recognised by the black colour being on the left of the defect.
- “2-Polarisation” :  
movie of the twist of a negative defect with an initial shape  $\mu_-(t = 0) = 1$ .

### Pairs of defects

For these videos, the initial separating distance  $R_0 = 48$ , linear size of the system  $L = 100$  lattice spacings.  $T = 0$ . Hereafter, the reported shapes are understood to be the initial shapes, at  $t = 0$ .

- “3-XY annihilation” :  
Annihilation of a pair. XY equilibrium case :  $\sigma = 0$ . Note how the  $\theta$  field conserves its symmetry with respect to the defects cores along the process.
- “4a-enhanced annihilation mu0” :  
Enhanced annihilation of a pair  $\mu_+ = 0, \mu_- = \pi$  for  $\sigma = 0.3$ . Note how the  $\theta$  field loses its equilibrium symmetry along the process. The polarisation axis progressively grows in the direction of the positive defects. Until now, none of the defects move in space. Then the axis reaches the  $+1$  defect. At from this point, both defects run along the axis that now connects them until annihilation.
- “4b-enhanced annihilation mu0.2” :  
Enhanced annihilation of a pair  $\mu_+ = 0.2, \mu_- = \pi - 0.2$  for  $\sigma = 0.3$ . Here the initial shape of the positive defect  $\mu_+ = 0.2 \neq 0$  so the positive defect should, if it were isolated, decay to the sink state. It does indeed start to twist in the first instants of the movie but the negative defect rapidly polarises its surroundings: the polarisation axis reaches the positive defect before it actually has time to complete its twist. The two defects are now connected by the axis and eventually annihilate following the scenario described above for a pure source  $\mu_+ = 0$ .
- “5a-hindered annihilation mu pi” :  
Hindered annihilation of a pair  $\mu_+ = \pi, \mu_- = 0$  for  $\sigma = 0.3$ . Typical configuration where the axis of the negative defect grows perpendicularly, hindering the annihilation process.
- “5b-hindered annihilation mu pi-0.5” :  
Hindered annihilation of a pair  $\mu_+ = \pi - 0.5, \mu_- = 2\pi - 0.5$  for  $\sigma = 0.3$ . Since  $\mu_- \neq 0, \pi$  the polarisation axis (initially) grows obliquely. Yet, complex dynamics of the surrounding  $\theta$  field impose an effective force on the axis, such that it becomes perpendicular to the core-to-core direction. Thus, it is hard for the  $-1$  defect to move: the XY annihilation process is hindered.
- “6a-transverse motion mu pi2” :  
Transverse motion, for  $\mu_+ = \pi/2, \mu_- = 3\pi/2$  and  $\sigma = 0.3$ . The polarisation axis grows obliquely while the positive defect decays to a sink. The negative defect then follows the polarised path just created. It eventually places itself below the positive defect, because in this configuration the axis is now perpendicular to the core-to-core direction. We are now in a configuration that leads to the hindering of the annihilation process.
- “6b-transverse motion creation defects mu pi2” :  
Same initial configuration, but now for  $\sigma = 0.5$ . Note how the polarisation axis, separating two domains of opposite orientation becomes so thin that the natural elasticity of the  $\theta$  field cannot support the large gradients  $|\nabla\theta|$  at this location. It therefore breaks to relieve the local tension, creating a new pair of defects: the new  $+1$  is on the right and meets/annihilates with the old  $-1$ . The new  $-1$  follows the rest of the polarised axis and places itself below the  $+1$ , for the same reasons as explained above.
- “6c-transverse motion annihilation mu pi2” :  
Same initial configuration, but now for  $\sigma = 0.2, T = 0.12 T_{KT}$ . The negative defect first follows the path traced by the axis, then stabilises below the positive defect for the same reasons as explained above. The difference with the two previous videos is that the present one is at finite temperature, such that the thermal fluctuations help the defects to annihilate.

### Coarsening dynamics of the system

We provide 3 movies of a  $L = 200$  triangular lattice, at  $T/T_{KT} = 0.08$ .

- “7a-XY system sigma 0” :  
XY case:  $\sigma = 0$  The field around defects usually is isotropic and non-twisted. Defect annihilate pair by pair following the scenario shown for isolated pairs of defects.
- “7b-NRXY system sigma 0.15” :  
Non-reciprocal case:  $\sigma = 0.15$  . Note how positive defects twist and how negative defects grows their polarisation axes, creating straight lines in the system. Note how the behaviours seen at the level of a single pair of defect are still valid in this many-body system of defects.
- “7c-NRXY system sigma 0.3” :  
Non-reciprocal case:  $\sigma = 0.3$  . Same comments, but the effects are intensified.

### Miscellaneous

- “8a-NRXY propagation sigma 0.5” :  
Unidirectional propagation of gradients, as already observed by [48] .
- “9-XY-NRXY chain of sinks” :  
A chain of sinks +1 defects (and their corresponding  $-1$  defects with  $\mu_- = \pi$  ) is unstable in the equilibrium XY model (left) and stable for the NR XY model ( $\sigma = 0.3$ ). The video is at  $T = 0$  for visualisation purposes but the phenomenon exists at finite  $0 < T < T_{KT}$ .

### Implementation details

The code is written in Julia language and is accessible publicly on GitHub at [github.com/yrouzaire/NRXY-Model](https://github.com/yrouzaire/NRXY-Model). Visit [julialang.org](https://julialang.org) to install Julia.

### Equation of motion : adimensionalisation procedure

Under its most general form, the phase of a spin  $\theta_i$  follows the overdamped Langevin equation

$$\gamma \dot{\theta}_i(t) = J \sum_{j \in \partial_i} g(\varphi_{ij}) \sin(\theta_j - \theta_i) + \sqrt{2k_B T \gamma} \eta_i(t)$$

where  $J$  is the elastic constant,  $\gamma$  the damping coefficient,  $k_B$  the Boltzmann constant and  $\eta$  a unit gaussian delta correlated noise. Dividing by  $J$  leads to

$$\frac{\gamma}{J} \dot{\theta}_i(t) = \sum_{j \in \partial_i} g(\varphi_{ij}) \sin(\theta_j - \theta_i) + \sqrt{\frac{2k_B T \gamma}{J^2}} \eta_i(t).$$

We then normalise time  $\tilde{t} = tJ/\gamma$  and define  $\tilde{T} = k_B T/J$ . One thus obtains

$$\dot{\theta}_i(\tilde{t}) = \sum_{j \in \partial_i} g(\varphi_{ij}) \sin(\theta_j - \theta_i) + \sqrt{\frac{2\tilde{T} \gamma}{J}} \eta_i(\tilde{t}/J)$$

Finally, since the delta function in the variance of the white noise  $\eta_i$  satisfies  $\delta(ax) = \frac{\delta(x)}{|a|}$ , one obtains the dimensionless equation of motion:

$$\dot{\theta}_i(\tilde{t}) = \sum_{j \in \partial_i} g(\varphi_{ij}) \sin(\theta_j - \theta_i) + \sqrt{2\tilde{T}} \eta_i(\tilde{t}).$$



We numerically integrate this equation in time using the Euler-Maruyama update rule:

$$\theta_i(t + dt) = \theta_i(t) + dt \sum_{j \in \partial_i} g(\varphi_{ij}) \sin(\theta_j - \theta_i) + \sqrt{2dt \cdot \tilde{T}} \eta_i$$

where the timestep  $dt = 0.1/z$ , where  $z$  is the coordination number (the number of nearest neighbours) and  $\eta_i \sim \mathcal{N}(0, 1)$ .

### Numerical Implementation of the Square and Triangular Lattices

All the values of  $\theta_i$  are stored in a square matrix for numerical efficiency, even for the triangular lattice. The topology of the network is encoded in the definition of the nearest neighbours, as shown in Fig.5. The indices  $i = 1, \dots, L$  correspond to the rows and run from top to bottom. The indices  $j = 1, \dots, L$  correspond to the columns and run from left to right.

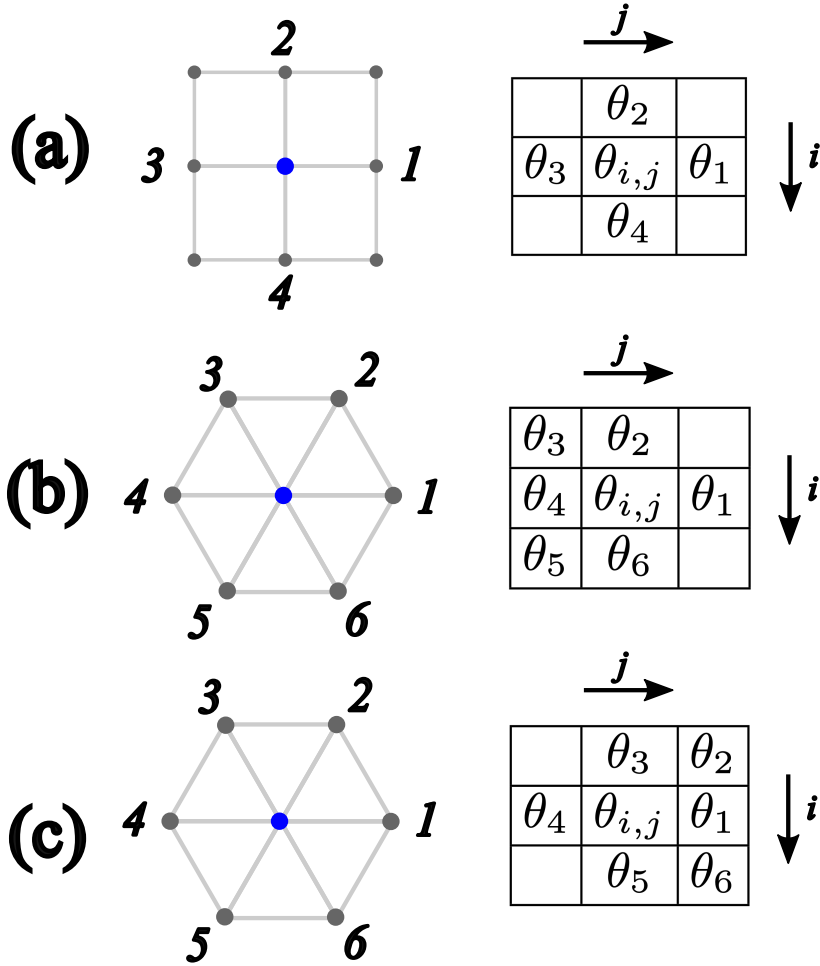


FIG. 5. Nearest neighbours structure for  
(a) square lattice, for all  $i, j$ .

(b) triangular lattice, for  $i$  even and all  $j$ .

(c) triangular lattice, for  $i$  odd and all  $j$ .

A triangular lattice can be thought as a square lattice with all odd rows laterally displaced by one half of the lattice spacing.

### Computation of the spatial correlation function

We define the spatial correlation function

$$C(r) = \langle \mathbf{S}_i \cdot \mathbf{S}_j \rangle = \langle \cos(\theta_i - \theta_j) \rangle \quad (4)$$

where spins  $i$  and  $j$  are separated by an euclidian distance  $r$ . The brackets  $\langle \cdot \rangle$  denote an ensemble average over thermal realisations (or equivalently, over all spins). Computing directly such a quantity in a  $L \times L$  system scales as  $\mathcal{O}(L^3)$ , which is prohibitive for large systems. For numerical efficiency, we compute it in the Fourier space, which reduces the numerical cost to  $\mathcal{O}(L^2 \log L)$ . First note that, by trigonometric identities,

$$\cos(\theta_i - \theta_j) = \cos(\theta_i) \cos(\theta_j) + \sin(\theta_i) \sin(\theta_j) \quad (5)$$

The term  $\cos(\theta_i) \cos(\theta_j)$  is a convolution and can be easily handled in Fourier space.

We note the Fourier transform operator  $\mathcal{F}$  and its inverse  $\mathcal{F}^{-1}$ . We note “ $\cdot^2$ ” the element-wise square operator: if  $x$  is a vector of components  $x_i$ , then  $x.^2$  is a vector of the same length of components  $(x_i)^2$ .

With this notation in mind, the  $2d$  spatial correlation function can be expressed as

$$C_{2d} = C(r_x, r_y) = |\mathcal{F}^{-1}(|(\mathcal{F}[\cos \theta])|^2 + (\mathcal{F}[\sin \theta])|^2)| \quad (6)$$

In a continuum simulation,  $C_{2d}$  would be a radial function. Here, because of the discrete nature of the underlying lattice,  $C_{2d}$  is slightly anisotropic. To obtain the usual unidimensional  $C(r)$ , we take the mean of the two principal components (along the axes) and normalise to get  $C(r=0) = 1$ .

### Constructing a pair of defects with controlled shapes

The first step to investigate an isolated pair of defects is to be able to create 2 defects with controlled shapes  $\mu_+$  and  $\mu_-$ . To do so, recall that around an ideal topological defect,  $\theta = q \arctan(y/x) + \mu$ . In polar coordinates, where

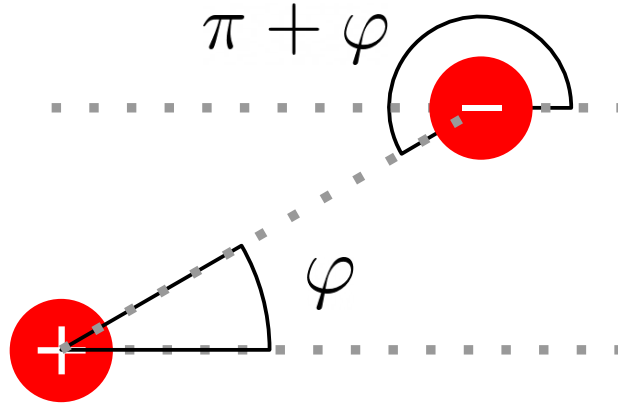


FIG. 6. Sketch of a pair of defects and definition of the polar angle  $\varphi$  that the negative defect makes with respect to the positive defect.

$\varphi = \arctan(y/x)$  (depicted in Fig.6), the field contribution from the defect reads  $\theta = q\varphi + \mu$ .

It follows that if one creates a positive defect with  $\mu_1$  and a negative defect with  $\mu_2$ , both fields will add up. At the location of the negative defect, the sum of the two contributions is

$$\mu_- = [\mu_1 + (+1)\varphi] + [\mu_2] = \mu_1 + \mu_2 + \varphi \quad (7)$$

At the location of the positive defect, the sum of the two contributions is

$$\mu_+ = [\mu_1] + [(-1)(\varphi + \pi) + \mu_2] = \mu_1 + \mu_2 - \pi - \varphi \quad (8)$$

Those are the concrete equations we use to create defects with controlled  $\mu_+, \mu_-, \varphi$  (only 2 of these 3 parameters are independent), tuning  $\mu_1 + \mu_2$  to obtain the desired  $\mu_+, \mu_-$ .

Also, one can get rid of the artificial  $\mu_1, \mu_2$  by combining these equations to obtain:

$$\mu_- - \mu_+ = \pi + 2\varphi. \quad (9)$$

As it creates the smoothest possible field, this equation represents the state of least distortion. It also highlights that only two of these three parameters are independent. In the main text, and without loss of generality, we work with  $\varphi = 0$ : the defects are horizontally aligned and the positive defect is on the left side.

### The defects' shape : definition, comments and analytic calculations

The field around a topological charge is given by the solution of the 2d Poisson equation:  $\theta(x, y) = q \arctan(y/x) + \mu$ . Once a defect is located, i.e. one knows  $(x_{core}, y_{core}, q)$ ; we then naturally define  $\mu = \text{Arg} \left\{ \sum_j \exp(i(\theta_j - q u_j)) \right\}$ , where the sum runs over the spins surrounding the plaquette of the dual lattice where the defect lies,  $i$  is the imaginary unit and  $\text{Arg}$  is the function that returns the phase of a complex number:  $\text{Arg}(re^{i\theta}) = \theta$ . Each neighbour  $j$  in that sum makes a certain angle  $u_j = \arctan(y_j/x_j)$  with respect to the horizontal axis. Irrespective of its position, we note its orientation  $\theta_j$ . We sketch this in Fig.7, where the red dots are the defects cores. For example, for the square lattice (left panel),  $u_j = j\pi/4$ ,  $j = 1, 2, 3, 4$ . For the upward (inner) triangular plaquette (central panel),  $u_{1,2,3} = \pi/2, -5\pi/6, -\pi/6$ . If the defect is located on a downward triangular plaquette (right panel), one has  $u_{1,2,3} = 5\pi/6, -\pi/2, \pi/6$ .

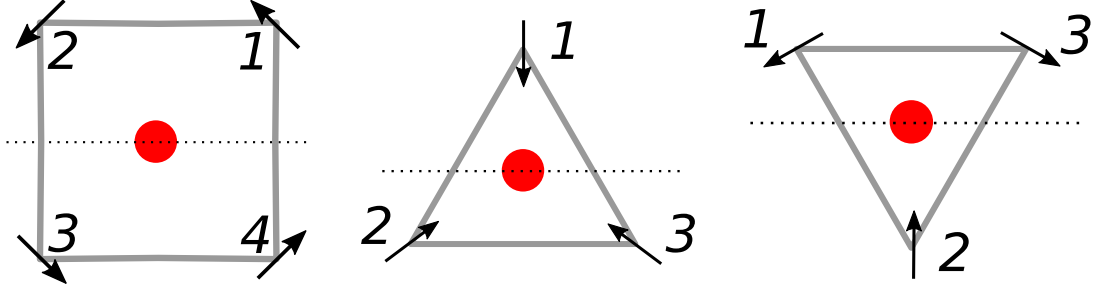


FIG. 7. Defects (red) lie at the centre of the dual plaquettes while the spins live on the lattice nodes (grey). Left panel: the unique plaquette of the square lattice. Centre and right panels: the two plaquettes (resp. up and down) of the triangular lattice. Dotted lines are horizontal and pass through the defects; the angles  $\theta_j$  and  $u_j$  are expressed with respect to that axis in the counterclockwise direction.

Note that  $\mu$  can be thought of as the value of the  $\theta$ -field at the immediate right side of the defect, as sketched in Fig.8 with the imaginary green arrows.

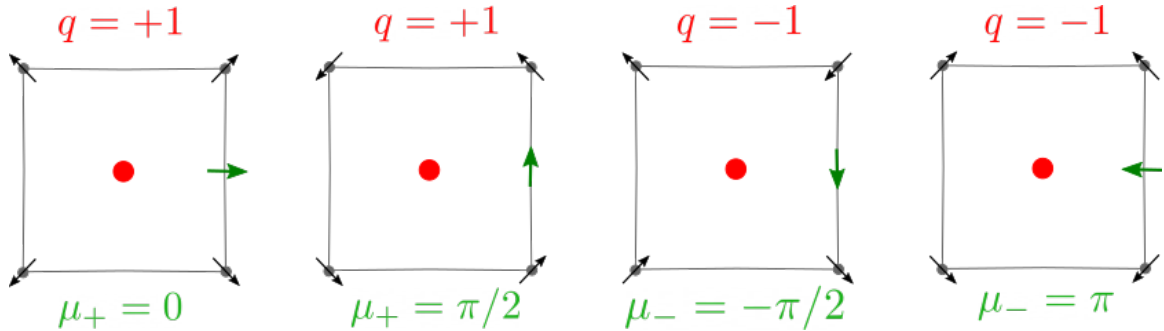


FIG. 8. The defects (red) live at the center of the dual plaquettes. The spins (black) live on the lattice, i.e. on the corners of the plaquette. An easy way to visually identify  $\mu$  is to imagine the orientation an imaginary spin (green) would have if located at the right edge of the defect ( $y = 0$  and thus  $\arctan(y/x) = 0$ ).

To support the intuitive argument sketched in Fig. 2(g,h) of the main text, we analytically compute the dynamics of the field around ideal isolated topological defects. We start from the equation of motion

$$\gamma \dot{\theta}_i = J \sum_{j \in \partial_i} g_\sigma(\varphi_{ij}) \sin(\theta_j - \theta_i) + \sqrt{2\gamma T} \eta_i(t) \quad (10)$$

We first study this dynamics in the continuum limit, where the orientation field is a function of a position  $\underline{x}$ , and consider a neighbourhood around this position. We also ignore noise and set  $J/\gamma = 1$  for simplicity.

$$\dot{\theta}(\underline{x}) = \int_{-\pi}^{\pi} g_\sigma(\phi_1 - \theta(\underline{x})) \sin(\theta(\underline{x} + \delta \hat{\phi}_1) - \theta(\underline{x})) d\phi_1 \quad (11)$$

Where  $\phi_1$  is the polar angle around position  $\underline{x}$  and  $\delta$  is a small finite distance which could be thought of as the inter defect spacing and  $\hat{\phi}_1$  is a unit vector with orientation  $\phi_1$ . This can now be re-written:

$$\dot{\theta}(\underline{x}) = \int_{-\pi}^{\pi} g_\sigma(\phi_1 - \theta(\underline{x})) \sin(\theta(\underline{x}) + \delta \hat{\phi}_1 \nabla \theta(\underline{x}) - \theta(\underline{x})) d\phi_1 \quad (12)$$

$$= \int_{-\pi}^{\pi} g_\sigma(\phi_1 - \theta(\underline{x})) \sin(\delta \hat{\phi}_1 \nabla \theta(\underline{x})) d\phi_1 \quad (13)$$

We now convert our coordinate system to polar coordinates around the center of a defect, which we denote  $(\phi, r)$  with corresponding orthonormal basis vectors  $[\hat{r}, \hat{\phi}]$  shown in the figure below.

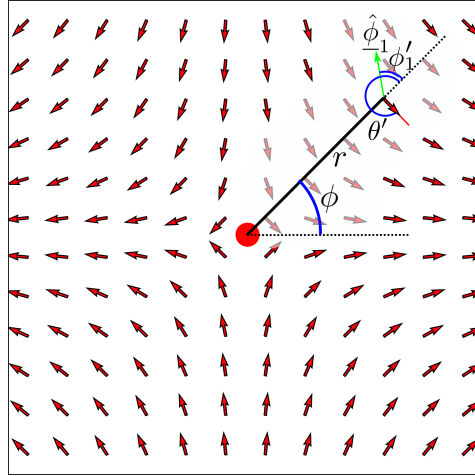


FIG. 9. Coordinate system for the calculation.

In this coordinate system, the new director field can now be written relative to the  $\hat{r}$  direction as:

$$\theta'(r, \phi) = \theta(\underline{x}) - \phi \implies \dot{\theta}' = \dot{\theta} \quad (14)$$

We must also convert the coordinate system over which we are performing the integration, thus:

$$\phi'_1 = \phi_1 - \phi \quad (15)$$

$$\hat{\phi}_1 = \cos(\phi'_1) \hat{r} + \sin(\phi'_1) \hat{\phi} \quad (16)$$

This leaves us at:

$$\dot{\theta}' = \int_{-\pi}^{\pi} g_\sigma(\phi'_1 - \theta') \sin(\delta \hat{\phi}_1 \nabla \theta(\underline{x})) d\phi'_1 \quad (17)$$

Note, we have not changed the limits of the integration as all functions are periodic over the interval  $[-\pi, \pi]$  so shifting by a constant does not change the integral.

Finally, we assume that  $\theta$  does not vary radially around a topological defect, thus  $\partial_r \theta' = 0$ . This is true for an isolated defect in the reciprocal XY model and allows us to write the gradient of  $\theta$  in the polar basis:

$$\nabla \theta = \frac{(\partial_\phi \theta' + 1)}{r} \hat{\phi} \quad (18)$$

Which gives us

$$\nabla \theta \cdot \hat{\phi}_1 = \frac{(\partial_\phi \theta' + 1)}{r} \sin(\phi_1) \quad (19)$$

Using these identities we can convert our equation to the new coordinate system to arrive at:

$$\dot{\theta} = \int_{-\pi}^{\pi} g_\sigma(\phi_1 - \theta) \sin \left( \delta(\partial_\phi \theta + 1) \frac{\sin(\phi_1)}{r} \right) d\phi_1 \quad (20)$$

Where we have dropped all '.

We consider the non-reciprocal kernel as  $g_\sigma(\varphi) = \exp(\sigma \cos(\varphi)) \approx 1 + \sigma \cos(\varphi)$  for small  $\sigma$ .

$$\dot{\theta} = \int_{-\pi}^{\pi} [1 + \sigma \cos(\phi_1 - \theta)] \sin \left( \delta(\partial_\phi \theta + 1) \frac{\sin(\phi_1)}{r} \right) d\phi_1 \quad (21)$$

$$= \int_{-\pi}^{\pi} \sin \left( \delta(\partial_\phi \theta + 1) \frac{\sin(\phi_1)}{r} \right) d\phi_1 + \sigma \int_{-\pi}^{\pi} \cos(\phi_1 - \theta) \sin \left( \delta(\partial_\phi \theta + 1) \frac{\sin(\phi_1)}{r} \right) d\phi_1 \quad (22)$$

### Stability of a +1 defect

For a +1 defect,  $\partial_\phi \theta' = 0$  and  $\theta' = \mu$ . With  $\mu = 0$  signifying a source and  $\mu = \pi$  being a sink. In this scenario there is no variance on the polar angle around the defect and we can write a single update equation for the shape of the defect  $\mu$ .

$$\dot{\mu} = \int_{-\pi}^{\pi} \sin \left( \delta \frac{\sin(\phi_1)}{r} \right) d\phi_1 + \sigma \int_{-\pi}^{\pi} \cos(\phi_1 - \mu) \sin \left( \delta \frac{\sin(\phi_1)}{r} \right) d\phi_1 \quad (23)$$

Since  $\sin \left( \delta \frac{\sin(\phi_1)}{r} \right)$  is anti-symmetric about  $\phi_1 = 0$ , the second integral will only give zero in the case where  $\cos(\phi_1 - \mu)$  is symmetric about zero. This is only true for  $\mu = 0, \pi$ , thus the only fixed points of this equation are these values.

We now linearize this equations around  $\mu$  using angle addition formula.

$$\Delta \dot{\mu} = \sigma \int_{-\pi}^{\pi} \cos(\phi_1 - \mu - \Delta\mu) \sin \left( \delta \frac{\sin(\phi_1)}{r} \right) d\phi_1 - \dot{\mu} \quad (24)$$

$$= \sigma \int_{-\pi}^{\pi} [\cos(\phi_1 - \mu) \cos(\Delta\mu) + \sin(\phi_1 - \mu) \sin(\Delta\mu)] \sin \left( \delta \frac{\sin(\phi_1)}{r} \right) d\phi_1 - \dot{\mu} \quad (25)$$

$$= \sigma \int_{-\pi}^{\pi} \cos(\phi_1 - \mu) \sin \left( \delta \frac{\sin(\phi_1)}{r} \right) d\phi_1 + \Delta\mu \sigma \int_{-\pi}^{\pi} \sin(\phi_1 - \mu) \sin \left( \delta \frac{\sin(\phi_1)}{r} \right) d\phi_1 - \dot{\mu} \quad (26)$$

$$= \Delta\mu \sigma \int_{-\pi}^{\pi} \sin(\phi_1 - \mu) \sin \left( \delta \frac{\sin(\phi_1)}{r} \right) d\phi_1 \quad (27)$$

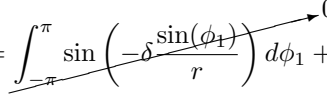
This is solved trivially by the equation  $\Delta\mu = A \exp[\omega t]$  with

$$\omega = \sigma \int_{-\pi}^{\pi} \sin(\phi_1 - \mu) \sin \left( \delta \frac{\sin(\phi_1)}{r} \right) d\phi_1 \quad (28)$$

Which indicates stability for  $\mu = \pi$  (sink) and instability for  $\mu = 0$  (source). The magnitude of  $\omega$  is greatest around  $r/\delta = 0.5$ , which means the evolution speed of  $\mu$  decreases as  $r$  increases (above the lattice spacing).

### Shape of a -1 defect

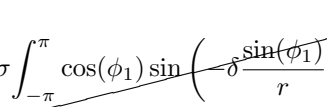
For a  $-1$  defect,  $\theta = -2\phi$  minimizes the energy in the reciprocal XY model. This is a defect in which the director points out along the  $x$  axis like the one shown in Fig. 9. This gives

$$\dot{\theta}(\phi) = \int_{-\pi}^{\pi} \sin\left(-\delta \frac{\sin(\phi_1)}{r}\right) d\phi_1 + \sigma \int_{-\pi}^{\pi} \cos(\phi_1 + 2\phi) \sin\left(-\delta \frac{\sin(\phi_1)}{r}\right) d\phi_1 \quad (29)$$


Once again the reciprocal terms vanish by symmetry. We can expand the second term using angle addition formula.

$$\dot{\theta}(\phi) = \sigma \int_{-\pi}^{\pi} \cos(\phi_1 + 2\phi) \sin\left(-\delta \frac{\sin(\phi_1)}{r}\right) d\phi_1 \quad (30)$$

$$= \sigma \int_{-\pi}^{\pi} [\cos(\phi_1) \cos(2\phi) - \sin(\phi_1) \sin(2\phi)] \sin\left(-\delta \frac{\sin(\phi_1)}{r}\right) d\phi_1 \quad (31)$$

$$= \cos(2\phi) \sigma \int_{-\pi}^{\pi} \cos(\phi_1) \sin\left(-\delta \frac{\sin(\phi_1)}{r}\right) d\phi_1 - \sin(2\phi) \sigma \int_{-\pi}^{\pi} \sin(\phi_1) \sin\left(-\delta \frac{\sin(\phi_1)}{r}\right) d\phi_1 \quad (32)$$


$$= \sin(-2\phi) \sigma \int_{-\pi}^{\pi} \sin(\phi_1) \sin\left(-\delta \frac{\sin(\phi_1)}{r}\right) d\phi_1 \quad (33)$$

This has quadrupole-like symmetry such that  $\theta$  will grow in the first and third quadrant, and shrink in the second and fourth, leading to a nematic symmetry of the  $-1$  defects. It is not easy to perform a similar linear stability analysis for the  $-1$  defect as the solution for  $\dot{\theta} = 0$  is non-trivial.

### Numerical results

We can estimate the stable solutions of Eq. 20 for different winding numbers using finite different methods. The winding number is fixed by the initial conditions and  $\theta$  is evolved using Eq. 20 until a stable solution is reached. The results are shown in Fig. 10 below.

### Symmetries of the system

The equilibrium XY model is invariant under global rotation of the spins  $\{\theta\} \rightarrow \{\theta + \alpha\}$  because the alignment term between two spins  $i$  and  $j$  only depends on the difference of the spins orientation:

$$\sin((\theta_j + \alpha) - (\theta_i + \alpha)) = \sin(\theta_j - \theta_i) \quad (34)$$

The reciprocal XY model is thus invariant under the addition of a global phase – we say it is  $O(2)$  invariant or, equivalently,  $O(2)$  symmetric– which prevents defects of the same topological charge but of different shapes (different phases) to behave differently.

In our 2D spin system, the parity transformation  $\begin{pmatrix} x \\ y \end{pmatrix} \rightarrow \begin{pmatrix} -x \\ y \end{pmatrix}$  can be re-expressed in terms of angles with the transformation  $\{\theta\} \rightarrow \{-\theta + \pi\}$ . Since the  $2dXY$  model is  $O(2)$  symmetric, we only have to check that the equation of motion is invariant under the transformation  $\{\theta\} \rightarrow \{-\theta\}$

$$\begin{aligned} \frac{d}{dt}(-\theta_i) &= \sin(-\theta_j - (-\theta_i)) \\ -\frac{d}{dt}(\theta_i) &= -\sin(\theta_j - \theta_i) \\ \frac{d}{dt}(\theta_i) &= \sin(\theta_j - \theta_i) \\ \dot{\theta}_i &= \sin(\theta_j - \theta_i) \end{aligned} \quad (35)$$



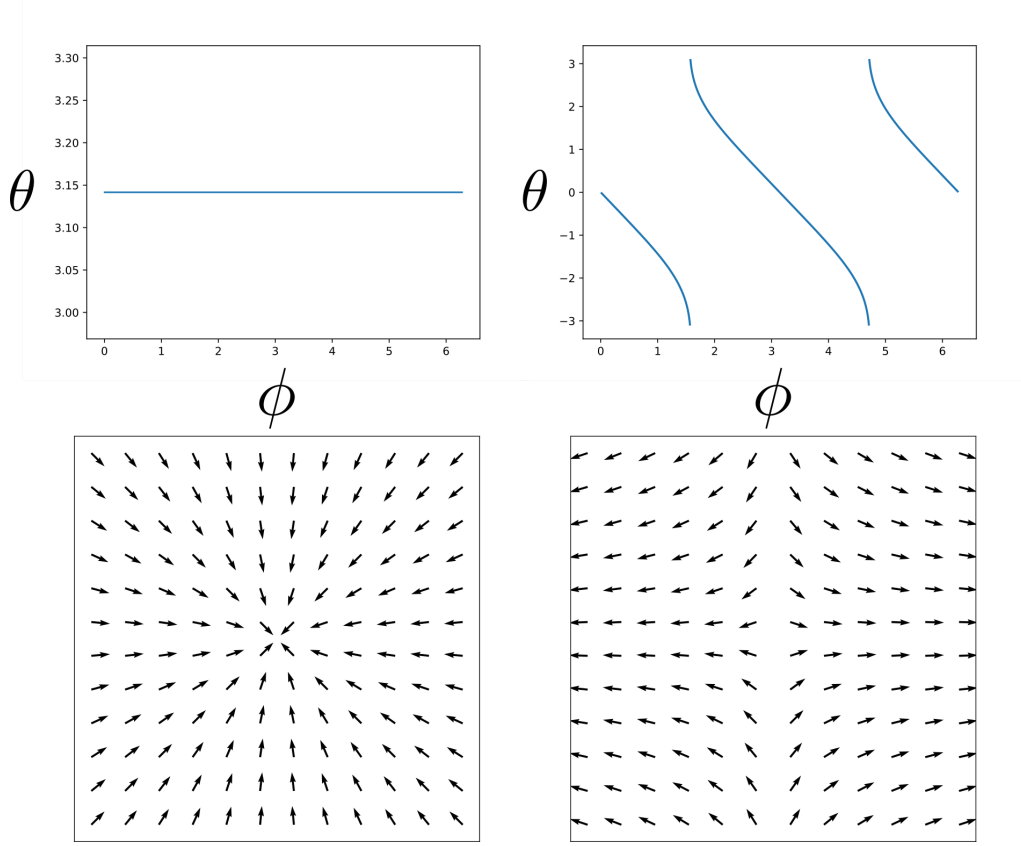


FIG. 10. Stable configurations for +1 (left) and -1 (right) defect. Both solutions obtained by numerically solving Eq. 20.

So the XY model is indeed invariant under parity. Note that the parity transformation transforms a  $q = +1$  defect into a  $q = -1$  and vice-versa, such that XY defects behave in the same fashion regardless of their charge.

On the other hand, the non-reciprocal kernel  $g$  violates all the previous symmetries. Indeed, while the alignment term depends on the difference of the spins orientation  $\theta_j - \theta_i$ ,  $g$  only depends on the orientation of the spin  $i$ . Therefore,  $g(\theta) \neq g(\theta + \alpha)$  and the system is no longer  $O(2)$  invariant. This is consistent with the results of the main text, where different shapes of the same topological charge (sinks and sources for +1 defects for example) behave in a totally different fashion. In the same spirit,  $g(\theta) \neq g(-\theta)$ , breaking parity. This is consistent with the difference in the dynamics between  $\pm 1$  defects in the non-reciprocal case. For instance, in the enhanced annihilation mechanism, positive defects move faster than negative defects, see Fig.3f of the main text.

Both claims are true for all kernels that do not depend on  $\theta_j - \theta_i$  but only on  $\theta_i$ .

### Kosterlitz-Thouless Critical Temperature

As described by Kosterlitz-Thouless theory [2, 3], the  $2dXY$  model exhibits a transition from a quasi-ordered phase to a disordered one, due to the unbinding of topological defects, at a temperature denoted  $T_{KT}$ .

At high temperatures  $T > T_{KT}$ , the entropy term wins and single isolated defects become energetically favourable: they proliferate and span the entire system, leading to disorder, characterised by exponentially decaying spatial correlation functions  $C(r) \sim e^{-r/\xi}$ , where  $\xi$  is the correlation length. At low temperatures, the only energetically favourable way for a defect to exist is to be bound with an oppositely charged defect, thus creating a pair. As the perturbation created by bounded defects gets limited to the distance between them, the system can reach quasi-long-range order, characterised by the power-law decay of spatial correlation functions  $C(r) \sim r^{-\eta}$ . In particular, at the transition temperature  $T = T_{KT}$ , renormalisation group calculations predict  $\eta = 1/4$ .

On the square lattice, the value of the critical temperature  $T_{KT} = 0.89$  has been deeply investigated [61, 62]. However, the literature is rather scarce regarding the triangular lattice case. Butera and Comi presented in 1994 a high-temperature expansion and concluded  $T_{KT} = 1.47$  [63]. Here, we directly measure the spatial correlation

function  $C(r)$  for different temperatures. The critical temperature  $T_{KT}$  is here determined as the largest temperature for which  $C(r)$  is well described by a power-law decay. We present the results in Fig.11(a) for the square lattice and Fig.11(b) for the triangular lattice. For the square lattice, we obtain  $T_{KT} = 0.89$ , in agreement with the reported values. For the triangular lattice, we obtain  $T_{KT} = 1.42$ , compatible with the value  $T_{KT} = 1.47$  reported in [63].

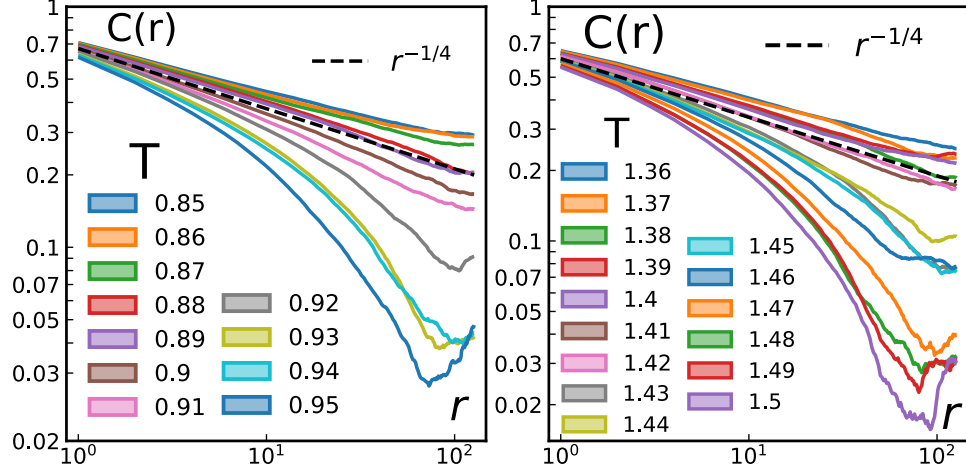


FIG. 11. Spatial correlation function  $C(r)$  computed for a  $L = 256$  system. (left) Square lattice, we obtain  $T_{KT} \approx 0.89$  (right) Triangular lattice, we obtain  $T_{KT} \approx 1.42$ .

Let's denote by  $T_4$  (resp.  $T_6$ ) the critical temperature for the square (resp. triangular) lattice. Interestingly, the ratio  $\frac{T_6}{T_4} = \frac{1.42}{0.89} = 1.60 \neq \frac{6}{4}$ , meaning that there is more going on than a simple rescaling due to the number of neighbours (as a simple mean-field treatment would predict).

### Growth of the polarisation axis with $\sigma$

Non-reciprocal interactions create large scale collective structures such as the polarisation axis of the  $q = -1$  defects. The larger  $\sigma$ , the more influenced spins are by the neighbours they look at. This favouring large coherent structures and the growth of the polarisation axis is faster for larger  $\sigma$ .

To quantify such process, one indirect but simple and informative measure is to monitor the *nematic* order parameter  $Q = \frac{1}{N} \sum_j e^{2i\theta_j}$ . We show in Fig.12 the time evolution of  $Q$  for a system composed of a single negative defect (centered). The initial condition is a perfectly isotropic defect  $\theta(x, y) = -\text{atan}(y/x) + \mu_-$ ,  $Q(t = 0) = 0$ ,  $P(t = 0) = 0$ . With time, the polarisation axis extends, separating two regions in which the *polar* order  $P$  increases (spins synchronise). Yet, those two regions have opposite orientation, so the global  $P$  remains zero throughout the process. However, the nematic order parameter  $Q$  increases as the contributions from the two regions add up. The left panel of Fig.12 shows that the larger the non-reciprocal parameter  $\sigma$ , the faster the dynamics. The right panel of Fig.12 shows the same data but as a function of  $\sigma t$  (in a logarithmic scale to emphasis the short time regime). Because the curves collapse at small times, we conclude that  $\sigma$  entirely controls the small time growth of the axis. However, the long time regime also depends on the elasticity of the  $\theta$  field, and hence how thin the polarisation axis can be. The larger  $\sigma$ , the thinner the axis can be (because the non-reciprocal forces dominate over the elastic ones), so the system tends to be fully polarised and  $Q(t \rightarrow \infty)$  increases.

Finally, the value of  $\mu_- = \text{Arg}(\sum_{j=1}^3 e^{i[\theta_j + \text{atan}(y_j/x_j)])}$  remains constant throughout this polarisation process. Indeed, even though the shape dramatically changes, losing its radial symmetry and almost gaining a translational symmetry, the field around a negative defect never loses its central symmetry, ie. the contributions from opposite quadrants (the origin being the defect core) remain equal and opposite. This implies that the value of  $\mu_-$  (the way we defined it) does not vary.

### Derivation of Eq. (2) and Eq. (3)

In this section, we detail the steps to write the equation of motion  $\dot{\theta}_i = \sum_j \sin(\theta_j - \theta_i) g(\varphi_{ij})$  in a continuous form, based on derivatives of the field  $\theta = \theta(x, y)$ , which emphasis the reciprocal and non-reciprocal contributions of

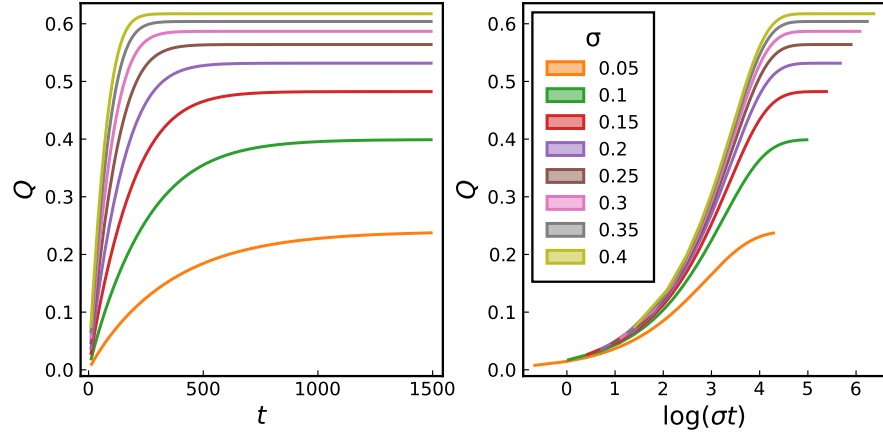


FIG. 12. **(left)** Nematic order parameter  $Q(t)$  of an isolated defect in a  $50 \times 50$  system at  $T = 0$ . Different colours correspond to different  $\sigma$ , as indicated in the right panel. **(right)** Same data, but against  $\log(\sigma t)$  instead of  $t$ .

the kernel.

Consider a spin  $i$  on the square lattice: it has 4 nearest neighbouring spins  $j = 1, 2, 3, 4$  (right, top, left, bottom), the orientations of which we note  $\theta_{1,2,3,4}$ . Those 4 neighbours can be thought to lie on a unit circle centred on the spin  $i$ . We call  $u_j$  the angle formed by horizontal axis and the location of spin  $j$ , see Fig.1a of the main text. In a square lattice,  $u_j = \frac{\pi}{2}(j-1)$ ,  $j = 1, \dots, 4$ . In a triangular lattice,  $u_j = \frac{\pi}{3}(j-1)$ ,  $j = 1, \dots, 6$ . Note that  $u_j$  and the orientation  $\theta_j$  are independent.

We start by explaining how *not* to proceed. One could be tempted to identify, from the beginning,  $\theta_j - \theta_i$  with the first order derivative of  $\frac{\partial \theta}{\partial k}$  ( $k = x, y$ ). The issue is, if one takes the simplest case of the XY model, where the kernel  $g = 1$ , one would obtain

$$\begin{aligned} \dot{\theta}_i &= \sum_j \sin(\theta_j - \theta_i) \\ &= \sin\left(\frac{\partial \theta}{\partial x}\right) + \sin\left(\frac{\partial \theta}{\partial y}\right) + \sin\left(-\frac{\partial \theta}{\partial x}\right) + \sin\left(-\frac{\partial \theta}{\partial y}\right) \\ &= 0 \end{aligned} \tag{36}$$

for all fields  $\theta(x, y)$  without any assumption. The reason why all terms cancel is that implicitly, one here uses the non-centred numerical definition of derivatives, therefore saying that  $\frac{\partial \theta}{\partial x} = \theta_1 - \theta_i = \theta_i - \theta_3$ , where the last equality is incorrect in general and especially around a topological defect.

To avoid this problem, one has to go to second order (not surprising if one wants to account for an elastic term) and consider both the spins on the right-left (resp. top-bottom) of the spin  $i$  of interest. If one linearises the coupling

kernel to first order in  $\sigma$  ( $e^{\sigma \cos x} \approx 1 + \sigma \cos x$ ), one obtains:

$$\begin{aligned}
\frac{\gamma}{J} \dot{\theta}_i &= \sum_j \sin(\theta_j - \theta_i) g(\varphi_{ij}) \\
&= \sum_j \sin(\theta_j - \theta_i) [1 + \sigma \cos(\varphi_{ij})] \\
&= \sum_j \sin(\theta_j - \theta_i) [1 + \sigma \cos(\theta_i - u_j)] \\
&= \sum_j \sin(\theta_j - \theta_i) \left[ 1 + \sigma \cos\left(\theta_i - \frac{\pi}{2}(j-1)\right) \right] \\
&= \sin(\theta_1 - \theta_i) (1 + \sigma \cos \theta_i) \\
&\quad + \sin(\theta_2 - \theta_i) \left[ 1 + \sigma \cos\left(\theta_i - \frac{\pi}{2}\right) \right] \\
&\quad + \sin(\theta_3 - \theta_i) [1 + \sigma \cos(\theta_i - \pi)] \\
&\quad + \sin(\theta_4 - \theta_i) \left[ 1 + \sigma \cos\left(\theta_i - \frac{3\pi}{2}\right) \right] \\
&= \sin(\theta_1 - \theta_i) (1 + \sigma \cos \theta_i) \\
&\quad + \sin(\theta_2 - \theta_i) (1 + \sigma \sin \theta_i) \\
&\quad + \sin(\theta_3 - \theta_i) (1 - \sigma \cos \theta_i) \\
&\quad + \sin(\theta_4 - \theta_i) (1 - \sigma \sin \theta_i) \\
&= \sin(\theta_1 - \theta_i) + \sin(\theta_3 - \theta_i) + \sin(\theta_2 - \theta_i) + \sin(\theta_4 - \theta_i) \\
&\quad + \sigma \cos(\theta_i) (\sin(\theta_1 - \theta_i) - \sin(\theta_3 - \theta_i)) \\
&\quad + \sigma \sin(\theta_i) (\sin(\theta_2 - \theta_i) - \sin(\theta_4 - \theta_i))
\end{aligned} \tag{37}$$

One has (the same goes for the vertical direction with  $\theta_2$  and  $\theta_4$ ) :

$$\begin{aligned}
&\sin(\theta_1 - \theta_i) + \sin(\theta_3 - \theta_i) \\
&= 2 \sin\left[\frac{1}{2}(\theta_1 - 2\theta_i + \theta_3)\right] \cos\left[\frac{1}{2}(\theta_1 - \theta_3)\right]
\end{aligned} \tag{38}$$

$$\begin{aligned}
&\sin(\theta_1 - \theta_1) - \sin(\theta_3 - \theta_1) \\
&= 2 \cos\left[\frac{1}{2}(\theta_1 - 2\theta_i + \theta_3)\right] \sin\left[\frac{1}{2}(\theta_1 - \theta_3)\right]
\end{aligned} \tag{39}$$

Now, if one identifies the differences in the continuum as

$$\begin{aligned}
a \frac{\partial \theta}{\partial x} &= \frac{\theta_1 - \theta_3}{2} \\
a \frac{\partial \theta}{\partial y} &= \frac{\theta_2 - \theta_4}{2} \\
a^2 \frac{\partial^2 \theta}{\partial x^2} &= \theta_1 - 2\theta_i + \theta_3 \\
a^2 \frac{\partial^2 \theta}{\partial y^2} &= \theta_2 - 2\theta_i + \theta_4
\end{aligned} \tag{40}$$

one obtains

$$\begin{aligned}
\frac{\gamma}{J} \dot{\theta} &= \cos(a \theta_x) \sin\left(\frac{a^2}{2} \theta_{xx}\right) + \cos(a \theta_y) \sin\left(\frac{a^2}{2} \theta_{yy}\right) \\
&\quad + \sigma \left( \cos \theta \sin(a \theta_x) \cos\left(\frac{a^2}{2} \theta_{xx}\right) + \sin \theta \sin(a \theta_y) \cos\left(\frac{a^2}{2} \theta_{yy}\right) \right)
\end{aligned} \tag{41}$$

where  $\theta = \theta(x, y)$ ,  $\theta_k = \frac{\partial \theta}{\partial k}$  and  $\theta_{kk} = \frac{\partial^2 \theta}{\partial k^2}$ ,  $k = x, y$ .

From this expression, it is now clear that (i)  $\sigma$  cannot be absorbed in the time unit (ii) the dynamics is  $\mu$ -invariant (it only depends on derivatives of the field  $\theta$ ) if and only if  $\sigma = 0$ .

In this small gradients limit, one can approximate  $\cos \alpha \approx 1$  and  $\sin \alpha \approx \alpha$ . One thus obtains

$$\frac{\gamma}{J} \dot{\theta} = a^2 (\theta_{xx} + \theta_{yy}) + 2a\sigma (\cos(\theta) \cdot \theta_x + \sin(\theta) \cdot \theta_y) \quad (42)$$

The first two terms give the Laplacian operator  $\Delta$  that physically represents the elasticity of the  $\theta$  field. The last two terms can be rewritten as follows:

$$\cos(\theta) \cdot \theta_x + \sin(\theta) \cdot \theta_y = \partial_x(\sin \theta) - \partial_y(\cos \theta) = (\nabla \times \mathbf{S})_z \quad (43)$$

where  $\mathbf{S} = (\cos \theta, \sin \theta)$  is the spin vector field, thus leading to the result of the main text Eq. (2):

$$\frac{\gamma}{J} \dot{\theta} = a^2 \Delta \theta + 2a\sigma (\nabla \times \mathbf{S})_z \quad (44)$$

Note that here we have kept  $\gamma, J$  and  $a$ , even though  $\gamma = J = a = 1$  in the adimensionalized main text version, to highlight the unitless nature of  $\sigma$ .

Inspired by the formulation in Eq. (2) in terms of the field

$$\mathbf{S} = \begin{pmatrix} S_x \\ S_y \end{pmatrix} = \begin{pmatrix} \cos \theta \\ \sin \theta \end{pmatrix}, \quad (45)$$

we look for an equivalent formulation of Eq. (2) entirely in terms of  $\mathbf{S}$ . Importantly, for now the magnitude of  $\mathbf{S}$  still remains strictly fixed to  $|\mathbf{S}| = 1$ , such that  $\dot{\mathbf{S}} \perp \mathbf{S}$ . Indeed, one has:

$$\dot{\mathbf{S}} = \dot{\theta} \begin{pmatrix} -\sin \theta \\ +\cos \theta \end{pmatrix} = \dot{\theta} \begin{pmatrix} -S_y \\ +S_x \end{pmatrix} \quad (46)$$

We start by the elasticity term  $\Delta \mathbf{S} = \begin{pmatrix} \Delta S_x \\ \Delta S_y \end{pmatrix}$ :

$$\begin{aligned} \frac{\partial^2}{\partial x^2} S_x &= \frac{\partial^2}{\partial x^2} (\cos \theta) \\ &= \frac{\partial}{\partial x} \left( -\frac{\partial \theta}{\partial x} \sin \theta \right) \\ &= - \left( \frac{\partial^2 \theta}{\partial x^2} \sin \theta + \left( \frac{\partial \theta}{\partial x} \right)^2 \cos \theta \right) \\ &= - \left( \frac{\partial^2 \theta}{\partial x^2} S_y + \left( \frac{\partial \theta}{\partial x} \right)^2 S_x \right) \\ &= - \frac{\partial^2 \theta}{\partial x^2} S_y \end{aligned} \quad (47)$$

Where the last equality results from the approximation that we only consider first order gradients. Also,

$$\begin{aligned} \frac{\partial^2}{\partial x^2} S_y &= \frac{\partial^2}{\partial x^2} (\sin \theta) \\ &= \frac{\partial}{\partial x} \left( \frac{\partial \theta}{\partial x} \cos \theta \right) \\ &= \frac{\partial^2 \theta}{\partial x^2} \cos \theta - \left( \frac{\partial \theta}{\partial x} \right)^2 \sin \theta \\ &= \frac{\partial^2 \theta}{\partial x^2} S_x - \left( \frac{\partial \theta}{\partial x} \right)^2 S_y \\ &= \frac{\partial^2 \theta}{\partial x^2} S_x \end{aligned} \quad (48)$$

Similarly,  $\frac{\partial^2}{\partial y^2} S_x = -\frac{\partial^2 \theta}{\partial y^2} S_y$  and  $\frac{\partial^2}{\partial y^2} S_y = +\frac{\partial^2 \theta}{\partial y^2} S_x$ , such that

$$\Delta \mathbf{S} = \left( \frac{\partial^2 \theta}{\partial x^2} + \frac{\partial^2 \theta}{\partial y^2} \right) \begin{pmatrix} -S_y \\ +S_x \end{pmatrix} = \Delta \theta \begin{pmatrix} -S_y \\ +S_x \end{pmatrix} \quad (49)$$

On the other hand, one has :

$$(\nabla \times \mathbf{S}) \times \mathbf{S} = (\nabla \times \mathbf{S})_z \begin{pmatrix} -S_y \\ +S_x \end{pmatrix} \quad (50)$$

Combining both parts leads to

$$\begin{aligned} a^2 \Delta \mathbf{S} + 2\sigma a (\nabla \times \mathbf{S}) \times \mathbf{S} &= [a^2 \Delta \theta + 2\sigma a (\nabla \times \mathbf{S})_z] \begin{pmatrix} -S_y \\ +S_x \end{pmatrix} \\ &= \frac{\gamma}{J} \dot{\theta} \begin{pmatrix} -S_y \\ +S_x \end{pmatrix} \\ &= \frac{\gamma}{J} \dot{\mathbf{S}} \end{aligned} \quad (51)$$

Defining  $\tilde{\sigma} = 2\sigma a$ , one obtains

$$\frac{\gamma}{J} \dot{\mathbf{S}} = a^2 \Delta \mathbf{S} + \tilde{\sigma} (\nabla \times \mathbf{S}) \times \mathbf{S} \quad (52)$$

Finally, one can relax the hard constraint  $|\mathbf{S}| = 1$  and only softly enforce a preferred magnitude (here unity without loss of generality) via a Lagrange multiplier term  $\alpha(1 - \mathbf{S}^2)\mathbf{S}$ :

$$\frac{\gamma}{J} \dot{\mathbf{S}} = a^2 \Delta \mathbf{S} + \tilde{\sigma} (\nabla \times \mathbf{S}) \times \mathbf{S} + \alpha(1 - \mathbf{S}^2)\mathbf{S} \quad (53)$$

As  $\sqrt{J/\alpha}$  physically sets the defects core size, it has to be larger than the simulation mesh spacing. In the simulations of the continuum model, we use  $\alpha = 100$ ,  $J = 1$ , and typically  $L = 256$ . The mesh spacing is  $1/256 \approx 0.004$  while  $\sqrt{J/\alpha} = 0.1$ .

#### Rewriting the model of Ref. [50] in terms of vector calculus operators

In their work [50], Vafa considered the following equation:

$$\begin{aligned} \partial_t p &= \mathcal{I}(p) = -\frac{\delta \mathcal{F}(\{p\})}{\delta \bar{p}} + \lambda \mathcal{I}_\lambda(p) \\ &= 4\partial \bar{\partial} p + 2\epsilon^{-2} (1 - |p|^2) + \lambda(p\partial + \bar{p}\bar{\partial})p \end{aligned} \quad (54)$$

They defined

$$\begin{aligned} p &= p_x + ip_y \\ \bar{p} &= p_x - ip_y \\ \partial &= \frac{1}{2} (\partial_x - i\partial_y) \\ \bar{\partial} &= \frac{1}{2} (\partial_x + i\partial_y) \end{aligned}$$

Therefore



$$\begin{aligned}
4\partial\bar{\partial} &= (\partial_x - i\partial_y)(\partial_x + i\partial_y) = \partial_x^2 + \partial_y^2 = \Delta \\
2p\partial &= (p_x + ip_y)(\partial_x - i\partial_y) \\
&= p_x\partial_x + p_y\partial_y + i(p_y\partial_x - p_x\partial_y) \\
2\bar{p}\bar{\partial} &= (p_x - ip_y)(\partial_x + i\partial_y) \\
&= p_x\partial_x + p_y\partial_y - i(p_y\partial_x - p_x\partial_y)
\end{aligned}$$

$$\text{So } (p\partial + \bar{p}\bar{\partial})p = (\vec{P} \cdot \nabla)\vec{P} \quad \text{where} \quad \vec{P} = \begin{pmatrix} p_x \\ p_y \end{pmatrix}.$$

### Supplementary discussion on the work of Loos, Klapp and Martynec (Phys. Rev. Lett. , 2023)

In their article *Long-Range Order and Directional Defect Propagation in the Nonreciprocal XY Model with Vision Cone Interactions* (2023) [48], Loos, Klapp and Martynec introduced a similar 2dXY model with non-reciprocal couplings. In this section, we discuss the differences between both approaches.

#### Discretisation issues

In [48], a spin  $j$  is considered to be in the neighbourhood of a spin  $i$  if and only if  $j$  is in the vision cone of  $i$ . They use a sharp vision cone kernel, as described in orange in Fig.1, such that  $j$  is an interacting neighbour of  $i$  if and only if the angle between the orientation  $\theta_i$  of the spin  $i$  and the location  $u_j$  of the spin  $j$  is less than half of the vision cone  $\Theta$ .

Because the underlying lattice is *discrete*, the sharpness of the kernel induces undesirable artefacts which we illustrate here on a triangular lattice ( $z = 6$  is thus the coordination number of the lattice).

The main discretisation effect is the generic change in the number of neighbours as the system evolves in time. This aspect is discussed in depth in [48]. The case  $\Theta = 2\pi/z$ ,  $n = 1, \dots, z$ , illustrated in Fig.13(a,b), is helpful to understand the issue. If the orientation of a spin  $i$  is  $\theta_i = \pi/2$ ,  $i$  has 4 neighbours in its vision cone. If its orientation fluctuates by an infinitesimal amount, it immediately loses one neighbour. The same happens for all values of  $\Theta$ , as we sketch in Fig. 13(c,d) for an arbitrary vision cone amplitude. The consequence of this brutal change in the number of neighbours is important. If one works with a Monte-Carlo type of dynamics, since the energy is extensive (as opposed to intensive if normalised by the number of contributing neighbours) there exist  $z$  regions energetically favourable imposed by the symmetry of the underlying lattice. This strongly promotes a local alignment with the symmetry of the lattice.

If instead one works with a Langevin approach based on extensive (i.e. additive) forces, a similar problem remains. We illustrate in Fig. 13(e) a configuration where the blue spin (in the center) has only one neighbour within its vision cone, while the green spin (on the right) has two neighbours, among which the latter one in blue. The Langevin equation of motion looks like  $\dot{\theta}_i = \sum_j \sin(\theta_j - \theta_i) + \sqrt{2T}\nu_i$ . For the blue spin, the sum only contains one contribution while for the green spin, it contains 2 terms so it is potentially twice as big. However, the temperature  $T$  of the thermal bath is constant. The ratio between the thermal angular diffusion and the interacting force becomes then space and time dependent.

To avoid these issues, one could imagine normalising the energy (or the force in a Langevin-like approach) by the (time-dependent) number of neighbours within the vision cone. However, this introduces another source of non-reciprocity, as the force of green on blue is now twice the force of the blue on green, in absolute value. The introduction of this new source of non-reciprocity has been documented in [64].

These issues are a consequence of having a sharp vision cone kernel. On the contrary, the soft vision cone kernel used in the present work strongly attenuates them. Since the kernel  $g(\varphi) = \exp(\sigma \cos(\varphi))$  is continuous and differentiable, a small change in  $\varphi$  can only generate a small change in  $g$ . A relevant measure is the sum of the angular weights  $\mathcal{G}_i \equiv \sum_{j=1}^z g(\varphi_{ij})$ , as it relates to the maximum force a spin can feel. In particular, its dependence on  $\theta_i$  is related to the discretisation effects; its dependence on  $\sigma$  allows to understand the relative importance of the two terms in the equation of motion: alignment and thermal noise. We have seen above that, in the sharp vision cone case, both a change in orientation  $\theta_i$  or in the vision cone amplitude  $\Theta$ , can result in a sudden gain of one neighbour, which translates in a sudden increase (+1) of  $\mathcal{G}_i$ . In the soft vision cone case, we want to study the dependence of  $\mathcal{G}_i$  on

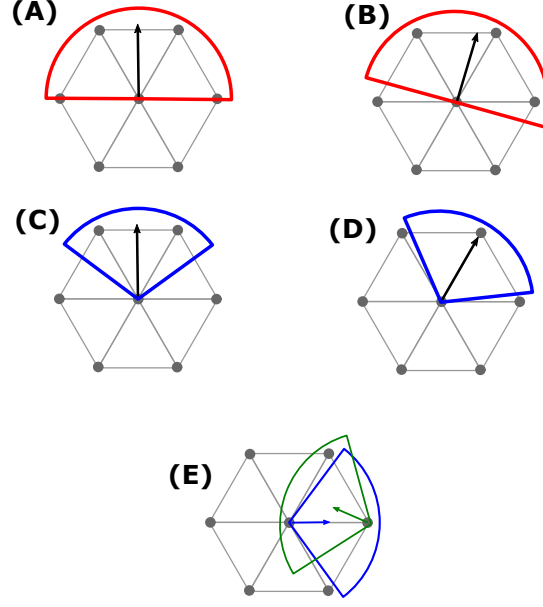


FIG. 13. **(A, B, C, D)** A spin can brutally lose or gain one neighbour within its sharp vision cone during the dynamics. **(E)** The effective temperature felt by two neighbouring spins can be different if their number of neighbours is different.

$\sigma$  and  $\theta_i$ . To do so, we consider the square lattice for two reasons: (i) the calculations are simpler (ii) discretisation effects in the triangular lattice are less pronounced than for the square lattice; we thus consider the worst case scenario. The sum over the angular weights gives:

$$\begin{aligned}
 \mathcal{G}_i &\equiv \sum_{j=1}^4 g(\varphi_{ij}) \\
 &= \sum_{j=1}^4 e^{\sigma \cos(\theta_i - u_j)} \\
 &= \sum_{j=1}^4 e^{\sigma \cos(\theta_i - (j-1)\frac{\pi}{2})} \\
 &= e^{\sigma \cos \theta_i} + e^{\sigma \sin \theta_i} + e^{-\sigma \cos \theta_i} + e^{-\sigma \sin \theta_i} \\
 &= 2 \cosh(\sigma \cos \theta_i) + 2 \cosh(\sigma \sin \theta_i)
 \end{aligned} \tag{55}$$

Since  $|\cos x| \leq 1$  and  $|\sin x| \leq 1$ , for small  $\sigma$  one can Taylor expand the cosh:

$$\begin{aligned}
 \mathcal{G}_i &= 2 + (\sigma \cos \theta_i)^2 + \frac{1}{12} (\sigma \cos \theta_i)^4 + \mathcal{O}(\sigma^6) \\
 &\quad + 2 + (\sigma \sin \theta_i)^2 + \frac{1}{12} (\sigma \sin \theta_i)^4 + \mathcal{O}(\sigma^6) \\
 &= 4 + \sigma^2 + \sigma^4 \frac{\cos^4 \theta_i + \sin^4 \theta_i}{12} + \mathcal{O}(\sigma^6)
 \end{aligned} \tag{56}$$

We learn that  $\mathcal{G}_i$  only varies with the orientation  $\theta_i$  to *fourth* order in  $\sigma$ . For  $\sigma = 0.5$ , it implies that  $\mathcal{G}_i(\theta)$  varies at most by 0.06 % from its maximum value  $\mathcal{G}_i(\theta = n\pi/2)$ ,  $n = 1, \dots, z$  (to be compared to the 100 % of the vision cone model when a spin passes from 1 to 2 neighbours). Indeed, when  $\theta = \pi/4$ , the mode of the kernel falls in between 2 neighbours, and

$$\begin{aligned}
& \frac{\mathcal{G}_i(\theta = 0; \sigma = 0.5) - \mathcal{G}_i(\theta = \pi/4; \sigma = 0.5)}{\mathcal{G}_i(\theta = 0; \sigma = 0.5)} \\
&= \frac{4.2552 - 4.2526}{4.2552} = 0.0006
\end{aligned} \tag{57}$$

Therefore, the soft vision kernel we propose indeed strongly attenuates the effects stemming from the underlying discrete lattice for the typical range of  $\sigma \in [0, 1/2]$  used in this work.

### Small vision cones and percolation threshold

Most of the results presented in this work are for values of  $\sigma \leq 0.5$ . We pushed up to  $\sigma = 1$  for Fig.3(e). However, one cannot increase  $\sigma$  up to arbitrarily large values. Indeed, the larger  $\sigma$  gets, the more peaked the kernel  $g(x) = \exp(\sigma \cos x)$  becomes. If almost all the mass of the distribution falls between two neighbours, the spin in fact “sees” no neighbour at all, and its dynamics is thus only driven by white noise. In this Letter, we work far from this regime. For instance, for  $\sigma = 0.5$ , the deviation from an isotropic kernel is moderate:  $g(0) = e^{0.5} \approx 1.65$  and the smaller coupling value is  $g(\pi) = e^{-0.5} \approx 0.6$ , far from negligible. Such pathological limit  $\sigma \rightarrow \infty$  is not a specificity of our model. Loos et al. [48], for their sharp vision cone model, report in the same spirit that for vision cones smaller than  $\pi/3$  on the triangular lattice ( $\pi/2$  on the square lattice), the percolation of the interaction network is no longer guaranteed.

### Comparison between sharp and soft vision cones

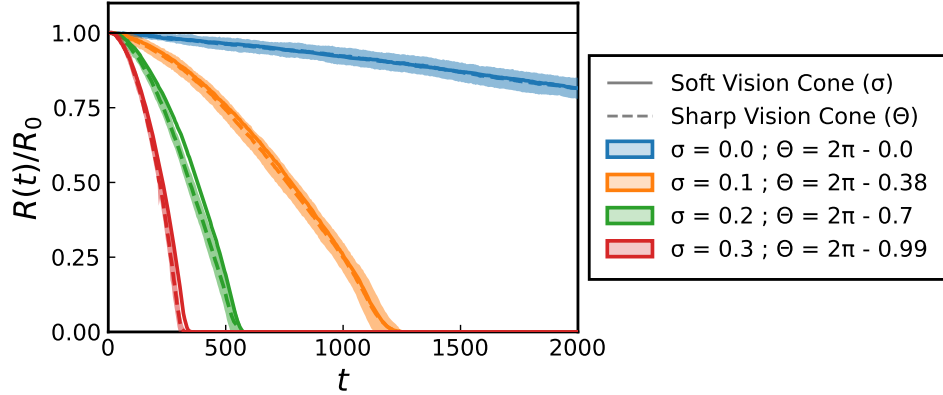


FIG. 14. Distance separating two defects over time in the enhanced annihilation configuration (the  $+1$  defect being a source  $\mu_+ = 0$ ). The annihilation dynamics of both models quantitatively match if the sharp vision cone aperture is taken from Eq.(62). Results for the sharp vision cone are averaged over  $R = 50$  independent realisations of the thermal noise. The standard deviations are shown with the ribbons.

For soft vision cones, we use the non-reciprocal parameter  $\sigma \geq 0$  used throughout the main manuscript. For sharp vision cones, we use a vision cone  $\Theta \leq 2\pi$ , centered on the phase  $\theta$  of the spins. Sharp and soft vision kernels ( $g_{\text{sharp}}$  and  $g_{\text{soft}}$ ) have a common property: the total weight in the head-side hemisphere ( $\varphi \in [-\pi/2, \pi/2]$ ) is greater than the total weight of the tail-side hemisphere ( $\varphi \in [\pi/2, 3\pi/2]$ ). We define the ratio  $f(\sigma)$  between those as

$$f(\sigma) = \frac{\int_{-\pi/2}^{\pi/2} d\varphi g(\varphi)}{\int_{\pi/2}^{3\pi/2} d\varphi g(\varphi)} \tag{58}$$

For a reciprocal (=isotropic) kernel  $g(\varphi) = 1$ , then  $f(\sigma) = 1$ ; while  $f(\sigma) > 1$  for non-reciprocal kernels.

*Soft vision cones*

For soft vision cones  $g_{\text{soft}}(\varphi) = \exp(\sigma \cos \varphi)$ , one obtains

$$f_{\text{soft}}(\sigma) = \frac{\pi(L_0(\sigma) + I_0(\sigma))}{\pi(L_0(\sigma) - I_0(\sigma))} \quad (59)$$

where  $L_0$  is the modified Bessel function of the first kind and  $I_0$  is the modified Struve function. For small  $\sigma$ , one can Taylor expand those functions up to second order to obtain

$$f_{\text{soft}}(\sigma) \approx \frac{\pi + 2\sigma + \pi\sigma^2/4}{\pi - 2\sigma + \pi\sigma^2/4} . \quad (60)$$

*Sharp vision cones*

For soft vision cones

$$g_{\text{soft}}(\varphi) = \begin{cases} 1 & \text{if } |\varphi| \leq \Theta/2 \\ 0 & \text{otherwise} \end{cases} ,$$

one obtains

$$f_{\text{sharp}}(\Theta) = \frac{\pi}{\Theta - \pi} . \quad (61)$$

Finally, equating the head-tail asymmetry ratios ( $f_{\text{sharp}} = f_{\text{soft}}$ ) gives an equivalence relation between  $\sigma$  and  $\Theta$ :

$$\Theta(\sigma) = 2\pi - \frac{16\pi\sigma}{\pi(4 + \sigma^2) + 8\sigma} \quad (62)$$

which allow to rationalise the dynamics of defects found in both versions of the model, as shown in Fig.14.

**Equation of motion stemming from the XY energy modulated by the kernel**

We now compare our Langevin equation of motion to the equation of motion one would obtain from the relaxation driven by an energy function

$$E = - \sum_{i,j} g(\varphi_{ij}) \cos(\theta_j - \theta_i) \quad (63)$$

If  $g(x) = \exp(\sigma \cos x)$ , the corresponding equations of motions would be ( $\Delta\theta_{ij} \equiv \theta_j - \theta_i$  and  $\varphi_{ij} \equiv \theta_i - u_j$ )

$$\begin{aligned} \dot{\theta}_i &= - \frac{\partial E}{\partial \theta_i} \\ &= - \sum_j \frac{\partial}{\partial \theta_i} (g(\varphi_{ij}) \cos(\Delta\theta_{ij})) \\ &= \sum_j g(\varphi_{ij}) \sin(\Delta\theta_{ij}) - \cos(\Delta\theta_{ij}) \frac{\partial g(\varphi_{ij})}{\partial \theta_i} \\ &= \sum_j g(\varphi_{ij}) \sin(\Delta\theta_{ij}) + \cos(\Delta\theta_{ij}) (\sigma \sin \varphi_{ij}) \underbrace{\frac{\partial \varphi_{ij}}{\partial \theta_i}}_{=1} g(\varphi_{ij}) \\ &= \sum_j g(\varphi_{ij}) \left[ \underbrace{\sin(\Delta\theta_{ij})}_{\text{attraction}} + \underbrace{\sigma \sin(\varphi_{ij}) \cdot \cos(\Delta\theta_{ij})}_{\text{(side) repulsion !}} \right] \end{aligned} \quad (64)$$

The first term  $\sin(\theta_j - \theta_i)$  corresponds to the alignment term in our Langevin description. The additional second term in  $\cos(\theta_j - \theta_i)$  favours orthogonal spin configurations, but, due to the  $\sin(\varphi_{ij})$  coefficient, this repulsion mainly takes place on the sides of the spin  $i$ , “ahead” being in the direction of  $\theta_i$ . The amplitude of this second term, however, is *a priori* smaller than the first term, since in this work we used  $\sigma \leq 1$  and since  $|\sin(\varphi_{ij})| \leq 1$ . Yet, the impact of this additional term, though only to second order, favours the stabilisation of the sources  $\mu_+ \approx 0$ , a configuration in which spins are indeed perpendicular.

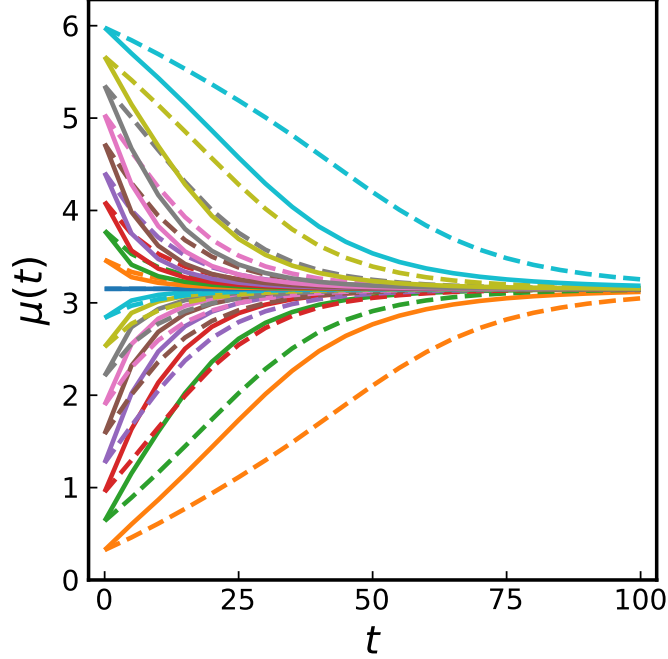


FIG. 15. In the spirit of Fig.2(i) of the main text, we monitor the shape  $\mu_+(t)$  of a positive defect over time, for different initial shapes  $\mu_+(0)$  (different colours). The solid lines correspond to our Langevin-based model, with only the first alignment term. The dashed lines correspond to equation Eq.(64), with the additional second term.

We report the effect of this additional term on the twist of positive defects in Fig.15. As stated, the  $\cos(\theta_j - \theta_i)$  term only has a small amplitude and thus does not change the stable configuration which remains the sink state  $\mu_+ = \pi$ . However, the decay to this stable state is slower, especially for initial configurations close to sources  $\mu_+ = 0 = 2\pi$  (cf. orange or cyan curves). This could have large-scale consequences, as the sources are the only defects involved in the enhanced annihilation process. If they are slightly stabilised by this repulsive term, the enhanced annihilation process could be even more dramatic and impact the overall coarsening dynamics.